NEAR EAST UNIVERSITY

Faculty of Engineering

Department of Electrical and Electronic Engineering

RADAR CROSS SECTION

Graduation Project
EE-400

Student: Mohammad Aamer Khan (991285)

Submitted to: Assoc. Prof. Dr. Sameer Ikhadir

Nicosia-2004

TABLE OF CONTENTS

ACKNOWLEDGEMENTS

I am absolutely thankful to the ALLAH all mighty who gave me the wisdom, strength and courage to complete my graduation project. I also thank my family for praying for my success and giving me economic support.

Studying in Near East University was a great of opportunity and I learned a great deal of knowledge and learned about life, especially the Turkish culture and hospitality was a nice and wonderful experience for me.

I am greatly thankful to my advisor Professor Mr. Ozgur, who has been my advisor since the last one and a half year.

To accomplish this task my respectful teacher and friendly project advisor Professor Dr. Sameer, who has guided me and helped me and made this memorable moments of my life easy to achieve. I am very thankful to Professor Dr. Sameer.

Some of my friends helped me a lot to get my job done, Mr. Arafat Issa and Mr. Munam Awais helped me a lot and made my stay at Near East University a wonderful experience.

ABSTRACT

The radar cross section σ is the property of a scattering object, or target, that is included in the radar equation to represent the magnitude of the echo signal returned to the radar by the target.

Sometimes radar cross section σ is said to be a (functional) area that intercepts a part of power incident at the target at which, if scattered uniformly in all directions, produces an echo power at the radar equal to that produced by the radar produced at the real target.

Radar cross section depends on the characteristic dimensions of the object compared to the radar wavelength. When the wavelength is large compared to objects dimensions, the scattering is said to be in Rayleigh region. It is named after Lord Rayleigh who first observed this type of scattering in1981, long before the existence of the radar, when investigating the scattering of light by microscopic particles. The radar cross section in Rayleigh region is proportional to the fourth power of frequency, and is determined more by the volume of the scattering than its shape. At radar frequencies, the echo from rain is usually described by Rayleigh scattering.

The spherical, cylindrical, flat plate, rod, ogive and cone are examples of simple targets. Analytically expressions exist for the radar cross section of some of these objects. Sometimes the radar cross section of complex targets can be calculated by describing the target as a collection of simple objects whose cross sections are known. The total cross section is obtained by summing vectorially the contributions from the individual simple shapes.

The cross section of complex targets such as aircrafts, missiles, ships, ground vehicles, fabricated structures, buildings and terrain can vary considerably depending on the view aspect and frequency. The variability results from the multiple individual scatterers that constitute the object. Each individual scatterer of a complex target produces an echo signal characterized by the amplitude and a phase. These echo signals combine at the radar to

produce the resultant signal. A change in the relative phase of the echo signal from the individual scatterer will occur if the relative position of the scatterer change with viewing aspect or there is a change in radar frequency.

It has been seen that the radar cross section of radar targets can vary with aspect, frequency and polarization. A single number is not a complete measure of radar cross section. There is no standard agreed upon methods for specifying the single value radar cross section of a target (probably because a single by itself is seldom used to describe a target). The average (mean) value or the median value might be taken. These depend on the probability density function that describes the fluctuations of the cross section.

INTRODUCTION

The importance of scattering of electromagnetic waves in the explanation of certain natural phenomenon was appreciated almost a century ago. During the past few decades, research in electromagnetic scattering by a variety of objects or targets assumed added importance because of its direct relevance to all radar applications and, in particular, to radars used for military and space explorations where the main objectives are to locate, identify, and classify various objects. The typical radar accomplishes these objectives by the processing of the received signals, which generally consists of the desired signal scattered by the target and the undesired noise or clutter signals, the former contains the information characteristics of the target. The receiver scattered signal power is directly proportional to the scattering of radar cross section (RCS) of the targets, hence the importance of the RCS of objects.

During the early years of the radar any acceptable methodology for calculation and on the analysis, computation, and measurement of RCS was considered adequate for radar engineering. Literature on the analysis, computation, and measurement of RCS is still extensive and still growing. With better understanding of electromagnetic scattering phenomenon it is a natural that consideration is now being given to deliberate control of RCS of objects for various applications. For example, with rapid advancements in missile and space technology attention increasingly is being directed towards disguising the presence of a flying object to unfriendly radar by reducing its RCS. Also, a demand seems to be appearing for the enhancement of RCS of communication and broadcast satellites so that they may be tracked better. The users of such satellites and other space objects may even request a complicated differential radar cross section as a function of the angular rotation of the objects or the swept of the frequency of the tracking radar. In short, the demand for the control of the RCS of various objects is increasing continuously due to its many military and civilian applications.

Apart form the estimation and measurement of RCS and its control required in the preceding applications, the RCS study finds important use in remote sensing and inverse scattering imaging. Although in the latter two areas some inversion algorithms generally are required, the input data are the complex scattered fields derived either from an experiment or by a suitable analytical model.

Because modern theoretical research on the RCS depend largely on the available compute power, it is appropriate to comment here on the role of the development of computer storage and speed on the capability of solving electromagnetic problems in general. Although the main frame computer power has grown at an approximately exponential rate, the prospect is not all that good for solving problems for electromagnetic scattering by large bodies, We cannot anticipate that the maximum target size handled would increase even in proportion with the present rate of increase in computer size and speed. However, innovative methods of fast processing of large matrices, parallel processing in computers, and concepts of neural networks may help the situation.

The measurement of RCS is no less important than the theoretical modeling. A modern computerized measurement facility can always provide a deeper insight into the scattering mechanism involved in simple as well as the complex targets. Recent advances in technology and measurement methods would complement the theoretical investigations to a great extent. Experimental facilities to a time-domain (wideband) measurement with windowing capability to filter out unwanted background reflections and other sources of noise and accurate near field sampling, and hence the far field sampling prediction, have been integrated in to a modern measurement system. These should greatly enhance the understanding of the subject of RCS and its control.

Here we are concerned primarily with the ways to control of the RCS of human made radar targets. A major difficulty in dealing with such a topic is that much of the work has not been published. Therefore we discuss the current state of the art in this area only within the confines of openly published literature and information.

The Radar Cross Section (RCS) is explained briefly in the five chapters.

The first chapter is introductory and describes the basic of electromagnetic field theory, the Maxwell's equations and the Wave equations are discussed. The Exact boundary conditions and the Impedance boundary concepts are discussed in order to provide the reader the basic knowledge of electromagnetic related to RCS.

The second chapter is related to the theory and its different aspects comprehensively and in detail about RCS. Some examples of RCS are given to have a better idea about the concept of RCS. How to predict RCS using exact methods and approximate methods are briefly discussed followed by RCS measurement techniques.

The third chapter deals with Radar Cross Section Enhancement. Some practical applications require enhancement of RCS; for example, when an aircraft or satellite is tracked. In this section it has also been discussed different practical devices for RCS augmentation, including their key design consideration.

The fourth chapter discusses the techniques of RCS reduction. It describes models leading to the design of low RCS targets and antennas. Case studies are represented to help the reader design low RCS objects.

In the last chapter, the conclusion has been described briefly.

CHAPTER 1

FUNDAMENTALS OF ELECTROMAGNETICS

1.1. Electromagnetic Theory Fundamentals And Introduction To Radar Cross Section

Study of any electromagnetic scattering problem requires a sound knowledge of basic electromagnetic theory, which may be found in many standard textbooks. For the benefit of the reader, a brief discussion of the fundamental laws and equations of electromagnetic including boundary conditions are discussed in this section.

1.1.1. Maxwell's Equations

Maxwell's electromagnetic field equations are mathematical descriptions of the four basic laws of electricity and magnetism. The word statements for these laws along with their mathematical representations follow.

(1) The electromagnetic force (emf) around a closed path L is equal to the negative of the magnetic displacement current through any stationary surface S enclosed by that path L (see Figure 1.1):

$$\oint_l \vec{E}\, dl = -\int_s \frac{\partial \vec{B}}{\partial t} \cdot \vec{ds} \ , \tag{1.1-a}$$

$$\nabla \times \vec{E} = -\frac{\partial \vec{B}}{\partial t} \ , \tag{1.1-b}$$

where E and B are the time and space dependent electric field intensity and magnetic flux density vectors, respectively. This is Faraday's law, which states that the induced emf in a closed circuit is equal to the negative of the time rate of increase of magnetic flux linked with that circuit.

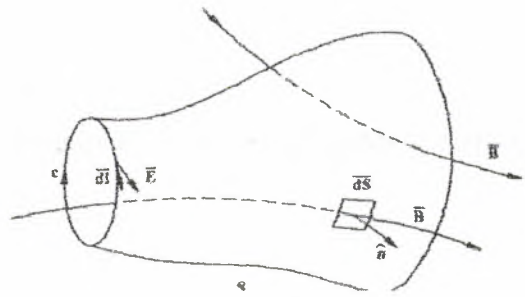

Fig.1.1. Surface S closed by a path L

(2) The magnefomotive force (rnmt) around a closed path L is equal to the total current through any stationary surface enclosed by that path L (see Figure 1.1):

$$\oint_L \vec{H}.\vec{ds} = \int_S \left(J + \frac{\rho \vec{D}}{\rho t} \right).\vec{ds} \quad , \tag{1.2-a}$$

$$\nabla \times \vec{H} = J + \frac{\partial \vec{D}}{\partial t} \quad , \tag{1.2-b}$$

where J is the electric volume current density that may include the applied current density when appropriate, and D is the electric flux density (or displacement) vector. This is Ampere's law as amended by Maxwell for the time varying case by introducing the displacement current density 8D/3 I to maintain the continuity of current.

(3) The total outward electric flux (or displacement) through a closed surface S enclosing a volume V is equal to the total electric charge contained within V:

$$\oint_S \vec{D}.\vec{ds} = \int v\rho_v \vec{ds} \quad , \tag{1.3-a}$$

$$\nabla.\vec{D} = \rho v \quad , \tag{1.3-b}$$

where the subscript V is the volume density of electric charge. This is a generalization of Gauss's law.

(4) The total outward magnetic flux through a closed surface S is always equal to zero:

$$\oint_S \vec{B}.\vec{ds} = 0 \ , \tag{1.4-a}$$

$$\nabla.\vec{B} = 0 \ , \tag{1.4-b}$$

This indicates that there is no isolated magnetic pole or charge and that the magnetic flux lines are always closed. Another law of considerable importance is the law of conservation of electric charge, which states that the total electric current flowing through a closed surface S is equal to the time rate of decrease of electric charge contained within the stationary volume V enclosed by S:

$$\oint_S J.\vec{ds} = -\int \vec{v} \frac{\partial \vec{dv}}{\partial t} \ , \tag{1.5-a}$$

$$\nabla.J = -\frac{\partial \rho v}{\partial t} \ , \tag{1.5-b}$$

Above equations together form the fundamental basis of electromagnetic theory. It is important to note that among these equations only (1.1), (1.2), and (1.5) are independent equations. All quantities in the preceding equations in general are real functions of space and time. In the time harmonic case, using pharos notations where it is assumed that all quantities are complex and space dependent and the time dependence is of the form exp(+ i , t), we can show [that the differential forms of the equations given earlier reduce to the following time-independent forms:

$$\nabla \times \vec{E} = -i\omega \vec{B} \ , \tag{1.6-a}$$

$$\nabla \times \vec{E} = J + i\omega \vec{B} \ , \tag{1.6-b}$$

$$\nabla.\vec{D} = \rho \vec{v} \ , \tag{1.6-c}$$

$$\nabla.\vec{B} = 0 \ , \tag{1.6-d}$$

$$\nabla . J + i\omega\rho v = 0 \quad , \tag{1.6-e}$$

In the presence of an isotropic material medium, the various field quantities are related to each other through the following constitutive relations:

$$\vec{D} = \varepsilon \vec{E} \quad , \tag{1.7-a}$$

$$\vec{B} = \mu \vec{H} \quad , \tag{1.7-b}$$

$$J = \sigma \vec{E} \quad , \tag{1.7-c}$$

Ordinarily the parameters ε, μ and σ characterizing a medium are real quantities. For a lossy dielectric medium we frequently find it convenient to use the notion of complex permittivity or (dielectric constant) represented (for e time dependence) by

$$\varepsilon = \varepsilon_O \varepsilon_r = \varepsilon_O \left(\varepsilon_r' - i\varepsilon_r''\right) \quad , \tag{1.8}$$

where ε_r' is the dielectric constant and accounts for the loss associated with the dielectric. The term ε_r'' is related to ε_r' through the loss tangent of the dielectric material defined as

$$\tan = \varepsilon'' / \varepsilon' \quad , \tag{1.9}$$

For a lossy dielectric having dielectric constant ε_r' and conductivity σ the following relationship holds,

$$\sigma = \omega \varepsilon_O \varepsilon_r'' \quad , \tag{1.10}$$

1.1.2. Wave Equations

In any electromagnetic problem the field quantities E and H must satisfy wave equations obtained from Maxwell's equations. For simplicity let us assume a source-free case involving an isotropic and homogeneous medium characterized by = $\mu = \mu_o \, \mu_r$ and $\varepsilon = \varepsilon_o \ \varepsilon_r$. After taking the curl (i.e., $\nabla \times$) of (1.6a) and using the vector identity $\nabla \times \nabla \times E = \nabla \cdot \nabla E - \nabla^2 \mathrm{E}$ and making use of (1.6b), (1.7a), and (1.7b) we obtain the time-independent homogeneous vector wave equation:

$$\nabla^2 \vec{E} - \gamma^2 \vec{E} = 0 \quad , \tag{1.11}$$

where γ is the complex propagation constant in the medium given by

$$\gamma = [i\omega\mu(\sigma + i\omega\varepsilon)]^{1/2} \tag{1.12}$$
$$= ik\left(1 - i\frac{\sigma}{\omega\varepsilon_0\varepsilon_r}\right)^{1/2} ,$$

$$k = k_0\sqrt{\mu_r\varepsilon_r} \quad , \tag{1.13}$$

The solution of (1.11) and (1.16) provides mathematical representation of an electromagnetic wave. Application of boundary conditions appropriate for a given problem then makes the solution unique. Thus, the boundary conditions play an important role in the solution of all electromagnetic problems. These are discussed next.

1.1.3. Exact Boundary Conditions

When an electromagnetic wave passes through an interface (or boundary) between two dissimilar media, the electric and magnetic field quantities in the immediate vicinity of the interface must satisfy certain identities or boundary conditions involving the fields, the material properties of the media, and the charge or current densities on the interface. These conditions can be obtained from the basic electromagnetic laws. Referring to Figure 1.2, we give without proof the boundary conditions on the tangential components of E and H, and the normal components of D and B at the interface between two media, where it is assumed that a surface charge density P and a surface current density J exist on the interface:

$$\hat{n} \times \left(\vec{E}_2 - \vec{E}_1\right) = 0$$

$$\vec{E}_{2t} = \vec{E}_{1t} \quad , \tag{1.17-a}$$

$$\hat{n}.(D_2 - D_1) = \rho s$$

$$D_{2n} - D_{1n} = \rho s \quad , \tag{1.17-b}$$

$$\hat{n} \times (H_2 - H_1) = Js$$

$$\vec{H}_{2t} - \vec{H}_{1t} = Js \quad , \tag{1.17-c}$$

$$\hat{n}.\left(\vec{B}_2 - \vec{B}_1\right) = 0$$

$$\vec{B}_{1t} = \vec{B}_{2t} \quad , \tag{1.17-d}$$

where t and n in the subscripts indicate the tangential and normal components, respectively.

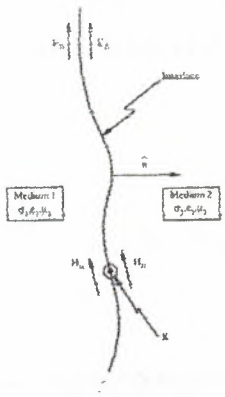

Fig.1.2. The interface between two dissimilar media.

It is important to note that in (1.10) P and J can be different from zero only when one of the media is conducting infinitely (i.e., a perfect conductor). Thus, at the interface of two media, neither of which is conducting infinitely, the tangential components of E and H and the normal components of D and B are continuous at the interface. The case of one of the media being perfectly conducting is of considerable practical importance and hence merits special treatment. Assuming a = 0, all field quantities in medium 1 are then equal to zero. Under these conditions, the boundary conditions at the interface between a perfectly conducting medium (medium 1) and a non-conducting medium (medium 2) reduce to

$$\hat{n} \times \vec{E} = 0, \hat{n}.\vec{D} = \rho s$$

$$\hat{n} \times \vec{H} = J_S, \hat{n}.\vec{B} = 0 \quad , \tag{1.18}$$

where we have removed the subscript 2 from the field quantities in medium 2.

1.1.3. Impedance Boundary Conditions

Problems of electromagnetic scattering from bodies that are imperfectly conducting, highly absorbing, conducting but coated with absorbing material, or conducting but with a rough surface are of considerable interest. In solving such problems we find it convenient to use an approximate boundary condition, named the impedance boundary condition (IBC) also known as the Leontovitch boundary condition. At the interface between such a body and the surrounding medium, the IBC is expressed as

$$\hat{n} \times \left(\hat{n} \times \vec{E} \right) = -Z_S \left(\hat{n} \times \vec{H} \right) \quad , \tag{1.19}$$

where

$\hat{n}$ = the unit normal directed into the surrounding medium,

E, H = the fields on the surrounding medium side,

Z = the surface impedance of the body defined as the ratio of tangential components of E and H on the surface.

As an example, for a plane wave traveling in the negative z-direction and incident on an imperfectly conducting material half-space defined by z is less than or equal to 0, (1.19) yields,

$$\vec{E_X} = -Z_S \vec{H_Y} \text{ and } \vec{E_Y} = Z_S \vec{H_X} \quad , \tag{1.20}$$

and in this case

$$Z_S = \frac{1+i}{\sigma \delta_S} \Omega \quad , \tag{1.21}$$

where $\delta_s = (2/\omega\mu_o\,\sigma)^{1/2}$ is the skin depth of the material.

The advantage of using the IBC is that it enables us to evaluate the scattered fields without knowing the fields inside the target. However, the IBC has its own limitations and region of validity. The possible errors involved in field calculations using the IBC depend on the assumptions made regarding the surface impedance. Figure 1.3 shows the region of validity of the IBC. It turns out that for a smooth surface, the exact boundary conditions can be replaced by IBC if

$$|Z_S| \rangle\rangle 1 \quad ,$$

$$\mathrm{Im}(N) \geq \frac{2.3}{k_O a} = \frac{2.3}{2\pi}\frac{\lambda}{a}, \lambda \langle\langle a \quad , \tag{1.22}$$

where N = $\sqrt{\mu_r \varepsilon_r}$ is the complex refractive index of the material of the scatterer, a is the minimum radius of curvature of its surface, and k is the free space propagation constant.

1.2. Typical Electromagnetic Scattering Problem

The geometry of a typical electromagnetic scattering problem is depicted in Figure 1 .4, where the transmitter (or source), usually located at a large distance from the target, illuminates the target, which now acts as a secondary radiator to produce scattered fields at the receiver or observation point P, also usually located at a long distance from the target. Monostatic or backscattering occurs when the transmitter and receiver are collocated, and bistatic scattering occurs when they are separated in space by an angle called the bistatic angel. Although the scattering results reported in the literature are predominantly Monostatic in nature, bistatic scattering also is Important to many applications.

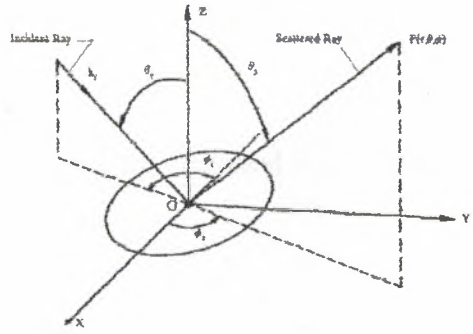

Fig.1.3. The electromagnetic scattering problem of radar target.

Depending on the size, shape, and the material constituent of the target, a wide variety of analytical techniques, is available for analysis of the scattering characteristics of a target. Generally, we try to determine the current distribution on the target induced by the incident field and then determine the scattered field as the field due to the induced current. For example, a smooth conducting body in free space illuminated by an electromagnetic wave will sustain an induced surface current distribution Js(r') where r' indicates the position vector of a point on the surface of the body. The magnetic vector potential A due to this current distribution at an observation point P whose position vector is denoted by r is,

$$\vec{A} = \frac{\mu_O}{4\pi} \int_S \frac{J_S(r') e^{ik_O|r-r'|}}{|r-r'|} \vec{ds} \quad , \tag{1.23}$$

where S is the total surface of the scattering body. With an incident plane wave E H', the high-frequency or physical optics approximation to current distribution is

$$J_S(r') = 2\hat{n} \times H^i \mathrm{Is} \quad , \tag{1.24}$$

with $\hat{n}$ as the unit positive normal at the surface. With knowledge of A, the scattered fields at P now can be obtained by using the following,

$$\vec{E^S} = -\frac{i\omega}{k_O^{\,2}} \left[k_O^{\,2} \vec{A} + \nabla\nabla . \vec{A} \right]$$

$$\vec{H}_S = \frac{1}{\mu_O}\left[\nabla \times \vec{A}\right] \quad , \tag{1.25}$$

In the far zone (i.e., $r \to \infty$), the scattered field expressions given above is simplify as follows:

$$\vec{E}^S = -i\omega \vec{A} \quad , \tag{1.25a}$$

$$\vec{H}^S = \vec{E}^S / \eta_O$$

As we can see, the fundamental task in all scattering problems is the determination of the induced current, which often is most difficult and cannot be obtained exactly. Frequently we formulate the problem in terms of an integral equation for the unknown current and then try to solve the equation either by approximate analytical methods or by numerical techniques.

Exact analytical determination of S often is very difficult, if not impossible, except for some simple targets. For most targets of practical interest approximate analytical or numerical techniques are used to determine S.

1.2.1. Near-Zone and Far-Zone Considerations

Near zone and far zone concepts play an important role in scattering by objects and in the design of measurement system for scattering. In the far zone of the target the scattered fields are orthogonal to the direction of energy propagation and their amplitudes decrease inversely with the distance from the target, whereas in the near zone there are nonzero components of the scattered fields in the direction of propagation and their amplitudes fall off faster than the inverse distance. There is no clear-cut definition for near-zone and far-zone boundaries. Customarily, an observation point is said to be in the near or far zone of the scatterer (target) if its distance from the scatterer is less or greater, respectively, than $2L^2/\lambda$ where L is the maximum dimension of the target; this criterion is based on the maximum allowable phase error of $\lambda/8$ or $\pi/4$ at the receiving aperture.

During measurement, the near-zone and far-zone question is decided by the requirements of the user and the minimum range to the target need not necessarily be $2L^2/\lambda$. Generally, the target or its model should be placed in the far zone if we want detailed information about the target. However, this may give rise to interference due to reflections from the floor, ground or multiple reflections from the surroundings. Using a range less than $2L^2/\lambda$, is not of great concern if we decide to use "average" values from the measurement.

In the area of antenna measurement, antennas with low side lobes have been found to require ranges longer than $2L^2/\lambda$ which is equally applicable to targets with low scattering side lobes. For many low- and ultra-low side lobe antennas or scatterers a practical range distance, such as $2L^2/\lambda$ still can be used to accurately measure wide angle side lobes, but at the expense of the first one or two side lobes.

1.3. Radar Cross Section

The IEEE definition of radar cross section is as follows: "For a given scattering object, upon which a plane wave is incident, that portion of the scattering cross section corresponding to a specified polarization component of the scattered wave." Clearly if the receiver is polarization matched to the scattered wave then the radar cross section and scattering cross section become identical, and we define the radar or scattering cross section in the direction (ϕ,φ), that is $\hat{r}$ (Figure 1.3) as

$$\sigma_s = \lim_{r\to\infty} 4\pi r^2 \left|\frac{E^S}{E^i}\right|^2 , \qquad (1.27)$$

where r is the distance from the target to the receiver and note that a has the dimension of area, that is, in square meters, m frequently, a is expressed as dBm with receiver in the far zone of the target. E^i and E^S are the incident and scattered (plane waves) electric fields respectively.

CHAPTER 2

THEORY OF RADAR CROSS SECTION (RCS)

2.1. The Concept of Echo Power

In order to calculate the degree of correlation and phase relation between the radar echo power and vertical velocity with respect to time, we decided to use the cross-spectral technique which has the added advantage that the results are sorted according to frequency.

2.1.1. Definition of RCS.

An object exposed to an electromagnetic wave disperses incident energy in all directions. This spatial distribution of energy is called *scattering,* and the object itself is often called a *scatterer.* The energy scattered back to the source of the wave called *(backscattering)* constitutes the *radar echo of* the object. The intensity of the echo is described explicitly by the radar cross section of the object, for which the abbreviation RCS has been generally recognized. Early papers on the subject called it the *echo area* or the *effective area,* terms still found occasionally in contemporary technical literature.

The formal definition of radar cross section is

$$\sigma = \lim_{r \to \infty} 4\pi R^2 \frac{\left|\vec{E}_S\right|^2}{\left|\vec{E}_O\right|^2} , \qquad (2.1)$$

where Es the electric-field strength of the incident wave impinging on the target where Eo is the electric-field strength of the scattered wave at the radar. The derivation of the expression assumes that a target extracts power from an incident wave and then radiates that power uniformly in all directions. Although the vast majority of targets do *not*

scatter energy uniformly in all directions, the definition assumes that they do. This permits one to calculate the scattered power density on the surface of sphere of radius R centered on the scattering object. R is typically taken to be the range from the radar to the target.

The symbol σ has been widely accepted as the designation for the RCS, although this was not so at first. The RCS is the projected area of a metal sphere which is large compared with the wavelength and which, if substituted object would scatter identically the same power back to the radar. The RCS of all but the simplest scatters fluctuates greatly with the orientation of the object. As such, this imaginary sphere would have to expand and contract with changing target orientation to represent the amplitude fluctuations displayed by most objects.

The limiting process in Equation (2.1) is not always an absolute requirement. In both measurement and analysis, the radar receiver and transmitter are usually taken to be in the far field of the target (discussed in Sec. (2.4), and at that distance the scattered field Es, decays inversely with the distance R. Thus, the R^2 term in the numerator of Equation (2.1) is canceled by an identical but implicit R^2 term in the denominator. Consequently the dependence of the RCS on R, and the need to form the limit, usually disappears.

Radar cross section is therefore a comparison of the scattered power density at the receiver with the incident power density at the target. An equally valid definition of the RCS results when the electric-field strengths in Equation (2.1) are replaced with the incident and scattered magnetic-field strengths. It is often necessary to measure or calculate the power scattered in some other direction than back to the transmitter, a bistatic situation. A bistatic RCS may be defined for this case as well as for back-scattering, provided it is understood that the distance R is measured from the target to the receiver. *Forward scattering* is a special case of bistatic scattering in which the bistatic angle is 180°, whence the direction of interest is along the shadow zone behind the target.

The shadow itself can be regarded as the sum of two fields of nearly equal strength but 180° out of phase. One is the incident field, and the other is the scattered

field. The formation of the shadow implies that the forward scattering is large, which is indeed the case. The fields behind the target are hardly ever precisely zero, however, because some energy usually reaches the shadow zone via diffraction from the sides of the target.

While there are few two-dimensional (infinite cylindrical) objects in the physical world, analyses of the scattering from two-dimensional structures are very useful. A two-dimensional object is, by definition, a cylinder formed by the pure translation of a plane curve to plus and minus infinity along an axis perpendicular to the plane of that curve. Many scattering problems become analytically tractable when there is no field variation along the cylindrical axis, such as when the infinite structure is illuminated by a plane wave propagating at right angles to the cylinder axis.

In this case, one defines a scattering *width* instead of a scattering area,

$$\sigma_{2D} = \lim_{\rho \to \infty} 2\pi\rho \frac{V_s^{\,2}}{V_o^{\,2}} \quad , \tag{2.2}$$

where ρ is the distance from the cylindrical body to a remove receiver, measured perpendicularly to the cylindrical axis. We have appended the subscript 2D to distinguish the scattering width of Equation (2.2), whose dimension is length, from the scattering cross section of Equation (2.1), whose dimension is the square of length.

By virtue of the linear properties of electromagnetic fields, the solutions of two-dimensional problems may be resolved into two cases, one each for the electric field or the magnetic field parallel to the cylindrical axis. The ratio $|V_s|/|V_o|$ thus represents either the incident and scattered electric fields or the incident and scattered magnetic fields, depending on the case at hand. These two cases are often called *E* and *H* polarizations, respectively. They are also known as TM and TH polarizations.

Practical three-dimensional problems often involve truncated segments of two-dimensional structures, such as shown in Fig. (2.1). In the practical world, those segments may be viewed at angles other than incidence perpendicular to the cylindrical axis, as implied in the solution of two-dimensional problems. The three-dimensional

RCS of a truncated two-dimensional structure may be found from the approximate relationship

$$\sigma = \frac{2l^2\sigma_{2D}}{\lambda}\left|\frac{\sin(kl\sin\tau)}{kl\sin\tau}\right|^2 , \qquad (2.3)$$

where l is the length of the truncated structure, σ_{2D} is its two-dimensional scattering width (obtained for the infinite structure), and τ is the tilt angle of the segment measured from broadside incidence. This approximation assumes that the amplitudes of the fields induced on the three-dimensional body are identically those induced on the corresponding two-dimensional structure and that the tilt angle influences only the phase of the surface fields induced on the body. The expression should not be used for large tilt angles, for which the amplitudes obtained from the two-dimensional solution no longer apply to the three-dimensional problem.

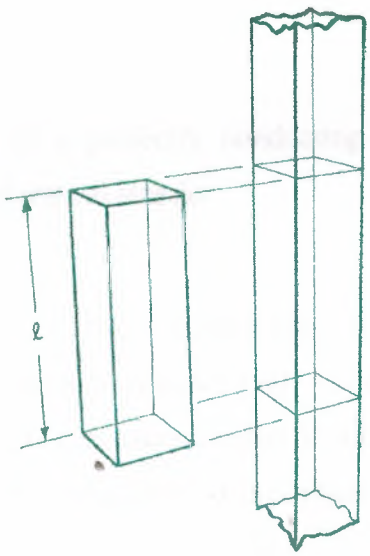

Fig.2.1 A three dimensional object whose profile does not vary along its length, such as the truncated rectangular cylinder on the left, is a finite chunk of a finite(two dimensional) structure having the same profile, such as the one on the right. Equation 2.3 relates the RCS of the two structures.

2.1.2. Examples of RCS Characteristics

Simple Objects. Because of its pure radial symmetry, the perfectly conducting sphere is the simplest of all three-dimensional scatterers. Despite the simplicity of its geometrical surface, however, and the invariance of its echo with orientation, the RCS of the sphere varies considerably with electrical size. The exact solution for the scattering by a conducting sphere is known as the Mie series, illustrated in Fig. 2.2.

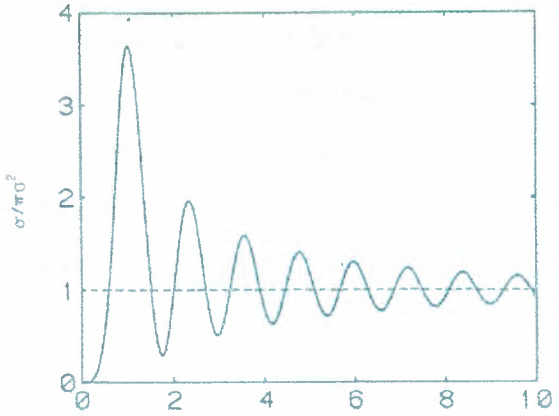

Fig. 2.2 RCS of a perfectly conducting sphere as a function of its electrical size *ka*.

The parameter $ka = 2a/\lambda$ is the circumference of the sphere expressed in wavelengths, and the RCS is shown normalizes with respect to projected area of the sphere. The RCS is shown rises quickly from a value of zero to a peak near $ka = 1$ and then executes a series of decaying undulations as the sphere becomes electrically large. The undulations are due to two distinct contributions

To the echo, one specular reflections from the front of the sphere and the other a creeping wave that skirts the shadow side. The two go in and out of sphere because the difference in their electrical path lengths continuously increasing *ka*. The undulations become weaker with increasing *ka* because the creeping wave loses more energy the longer the electrical path traveled around the shadowed side.

The log-log plot of fig 2.3 revels the rapid rise in RCS in the region $0< ka < 1$, which is know as Raleigh region. Here the normalized RCS increases with the Fourier power of ka, a feature shared by other electrically small or thin structures. The central region is characterized by the interference between the specular and creeping wave contribution is known as the *resonance region.*

The echoes of all scattering objects, and not just the perfectly conducting sphere, can be grouped according to the electrical-size characteristics of the object. The dimensions of a Raleigh scatterer are much less than a wavelength, and the RCS is proportional to the square of the volume of the body. Resonant scatterers are generally of the order of one-half to 10 wavelengths in size, for which neither Raleigh nor optics approximations may be very accurate. In the optics region several approximations are available for making estimates or pre-dictions (see Section 2.3).

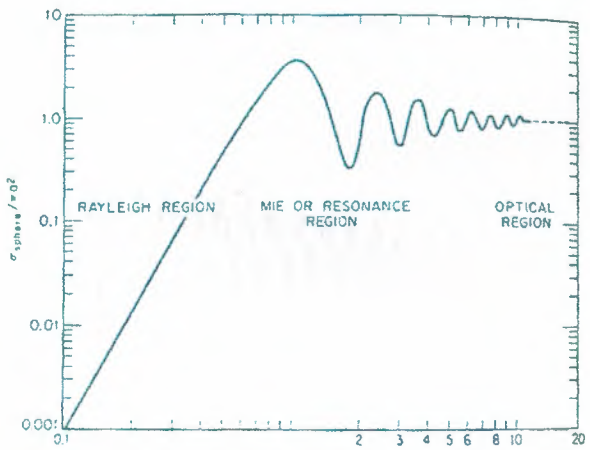

CIRCUMFERENCE/ WAVELENGTH= $2\pi a / \lambda$

Fig. 2.3 Log-log version of the data displayed in fig. 2.2.

The echo characteristics of permeable (dielectric) bodies can be more complicated than those of perfect conductors because energy may enter the body and suffer several internal bounces before emerging. An example is the dielectric sphere whose RCS is plotted in figure (2.4). Because the dielectric material is slightly lossy, as indicated by the nonzero imaginary component of the index of refraction, the RCS of the sphere

decays gradually with increasing electrical size. The RCS of small dielectric bodies does not exhibit this complexity, on the other hand, because the sources of reflection are too close to each other to be resolvable by the incident wave. An example is the two-dimensional Raleigh region RCS of a thin dielectric cylinder, plotted in figure (2.5). The thin dielectric cylinder has been used to model the target support lines sometimes employed in RCS measurements. Note that the *H*-polarized echo is barely 6 dB less than that for *E* polarization for this particular dielectric constant.

The thin wire (a metal dipole) can have a complicated pattern, as shown in figure (2.6). The RCS of the wire varies with the wire length, the angel subtended by the wire and the line of sight, and on that component of the incident electric field in the plane containing the wire and the line of sight. The wire diameter has only a minor influence if it is much larger than the wavelength. In addition to the prominent broadside lobe at the center of the pattern, there are traveling wave lobes near the left and right side. The traveling-wave lobes tend to disappear as the dipole becomes shorter and are closely related to those excited on traveling waves antennas.

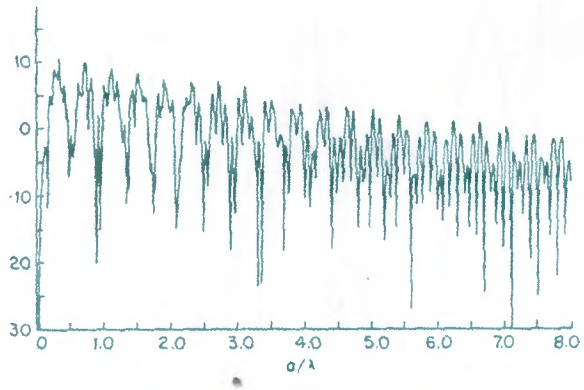

Fig.2.4. RCS of a lossy dielectric sphere with $n = 2.5 + i0.01$

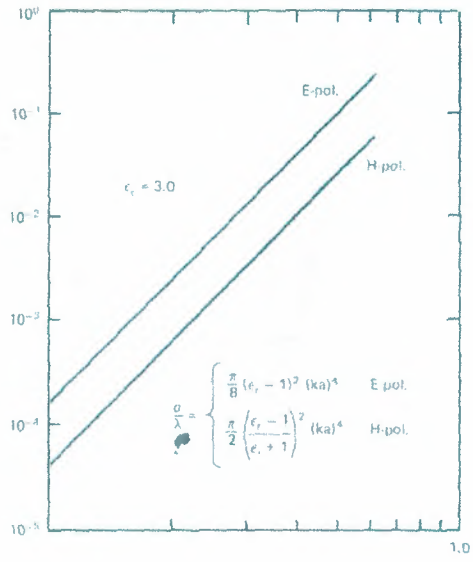

Fig.2.5. RCS of a slender dielectric cylinder with $\varepsilon_r = 3.0$

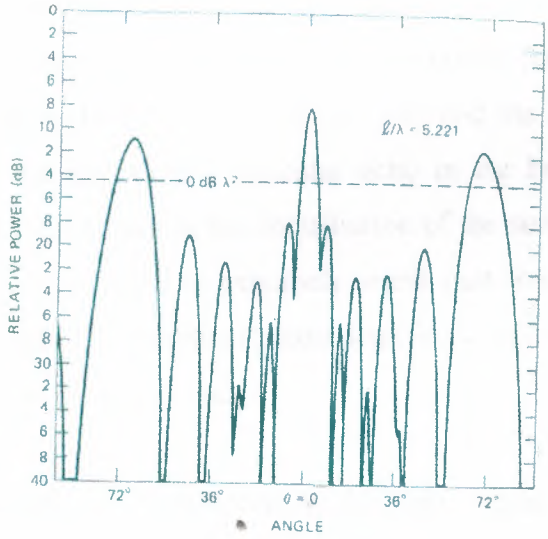

Fig.2.6. Measured RCS pattern of a dipole 5.221 λ long

Figure (2.7) shows the broadside resonance of a wire dipole as a function of dipole as a function of dipole length. The first resonance occurs when the dipole is just under a half dipole length long. And its magnitude is very nearly λ^2. Other resonance occurs near odd multiple of a quarter wave length, with plateaus of nearly constant return between the resonant peaks. These plateaus rise as dipole becomes thicker, and the resonances eventually disappear.

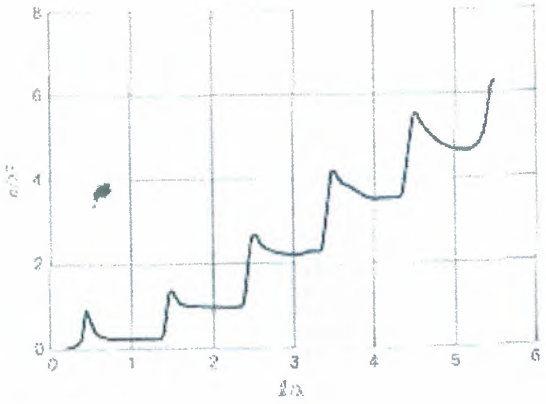

Fig.2.7. Measured broadside returns of a thin dipole.

Bodies considerably thicker than the thin wire also support surface traveling waves that radiate power in the backward direction. An example is the ogive, a spindle-shaped object formed by rotating an area of a circle about its chord. Figure 2.8, is the RCS pattern of a wavelength 15 half-angel ogive recoded for horizontal polarization (incident electric field in the plane of the ogive axis and the line of sight). The large lobe at the right of the pattern is a specular echo in the broadside sector, and the sequence of peaks at the left side is the contribution of the surface traveling wave near end-on incidence. Note the RCS is extremely smell (not measurable in this case) at precisely end-on incidence. Theoretical predictions in the end-on region closely match the measured pattern for particular body.

The dominant scattering mechanisms for the right circular conducting cone are the tip and the base. The return from the tip is very small in the nose-on region and the RCS pattern is dominated by the echo from the base. Figures (2.9) and (2.10) are patterns of the RCS of a 15° (half-angle) cone with a base circumference of 12.575X. Both patterns were measured as the cone was rotated about a vertical axis parallel to the base of the cone. The transmitted and received electric polarization was in the plane swept out by the cone axis (horizontal polarization) for Figure (2.9) and was perpendicular to that plane (vertical polarization) for figure (2.10).

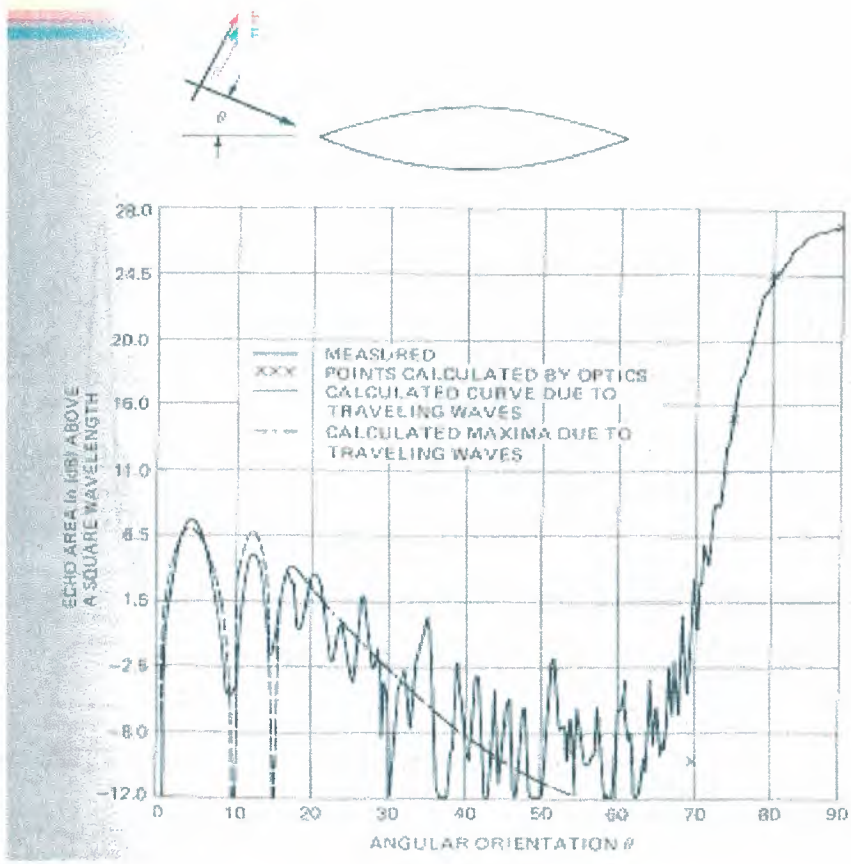

Fig.2.8. measured RCS patterns of a 39-wavelength 15 half-angle metal ogive.

Nose-on incidence lies at the center of the patterns, and the sharp peaks near the sides are the specular returns from the slanted sides of the cone, also called specular *flashes.* The RCS formula for singly curved surfaces given in table (2.1) may be used to predict the amplitudes of the specular flash within a fraction of a decibel. At precisely nose-on incidence the RCS must be independent of polarization because the cone is a body of axial symmetry. This may be verified by comparing the nose-on values in the two figures. At this angle the entire ring of the base of the cone is excited, but as the aspect angle swings away form nose-on,

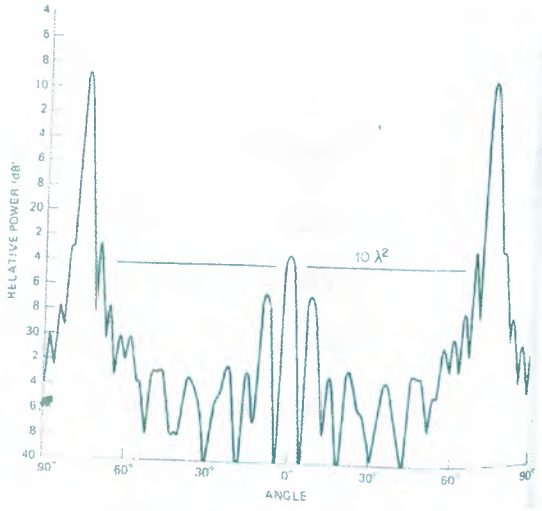

Fig.2.9. Measure RCS of a 15 half-angel cone (horizontal polarization), The base circumference s 12.575 λ. The heavy horizontal line indicates 10 λ^2.

The scattering from the base degenerates to a pair of flash points. They lie at opposite ends of a diameter across the base in the plane containing the direction of incidence and the cone axis.

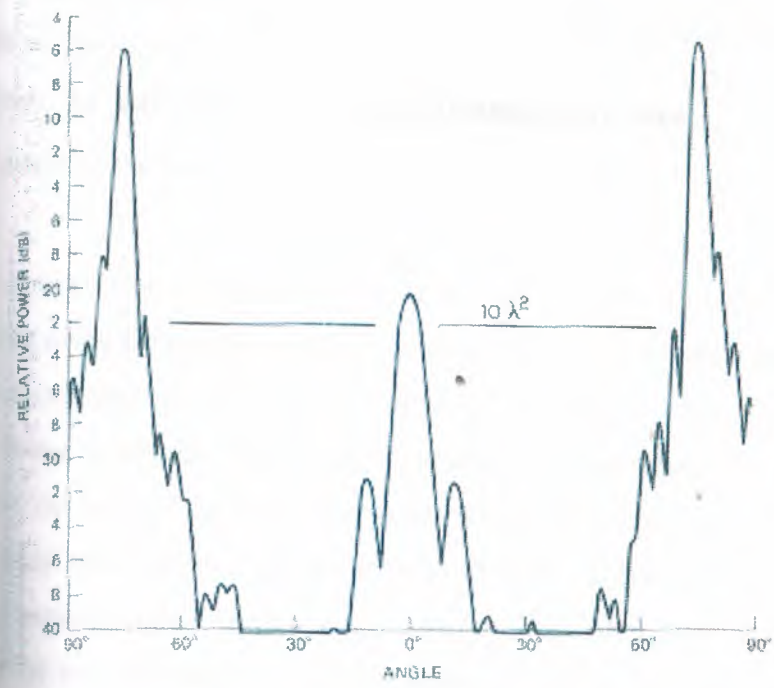

Fig.2.10. Measured RCS of a 15 half angle cone (vertical polarization). The base circumference is 12.75λ. The heavy horizontal line indicates10λ^2.

Scattering Features	Orientation	Approximate RCS
Corner reflector	Axis of symmetry along LOS	$4\pi A_{eff}^2 / \lambda^2$
Flat plate	Surface $\perp$ to LOS	$4\pi A^2 / \lambda^2$
Singly curved surface	Surface $\perp$ to LOS	$2\pi a l^2 / \lambda$
Doubly curved surface	Surface $\perp$ to LOS	$\pi a_1 a_2$
Straight edge	Edge $\perp$ to LOS	l^2 / π
Curved edge	Edge element $\perp$ to LOS	$a\lambda / 2$
Cone tip	Axial incidence	$\lambda^2 \sin^4(\alpha / 2)$

where,

LOS = Line of sight.

A_{eff} = Effective area contributing to multiple integral reflection.

A = Actual area of the plate.

a = Mean radius of curvature.

l = Length of slanted surface.

a_1, a_2 = Principle radii of surface curvature in orthogonal plane.

α = Half angle of the cone.

The echoes from the flash points at the sides of the base weaken as the aspect angle moves away from nose-on incidence, and the side lobes seen at +13° are actually due to an interaction between the two flash points *across the shadowed side* of the base. (The side lobes disappear when a pad of absorber is cemented to the base.) The flash point at the far side of the base disappears when the aspect angle moves outside the backward half cone, but the near flash point remains visible, and its echo decays with increasing aspect angle. Trailing-edge contributions like these are excited by that component of the incident electric field perpendicular to the edge; therefore they are stronger for horizontal incident polarization than for vertical polarization.

A flat plate also can support multiple diffraction from one side of the plate to the other, as shown in figure (2.11). The axis of rotation was in the plane of the plate

parallel to one edge; normal incidence to the incident wave is 0°, at the left side of each chart, with edge-on incidence at 90° near the right side. The specular return from the plate is the large peak at 0°, which is predicted with quite good accuracy by the flat-plate formula given in Sec. (2.3). The edge-on return for vertical polarization is well predicted by the straight-edge.

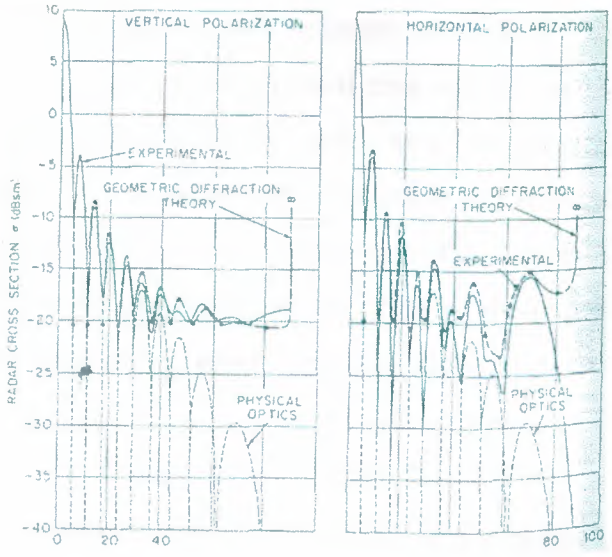

Fig.2.11. RCS of a square flat plate 6.5 inch long a side; $\lambda = 1.28$ inch

These undulating patterns follow a sin x/x variation quite closely for aspect angles out to about 30°, but beyond that angle the two patterns differ by progressively wider margins. The sin x/x behavior is characteristic of a uniformly illuminated aperture, but unlike the one-way illumination function encountered in antenna work, the argument x for a flat plate includes a two-way (round-trip) illumination function. Thus, the beam width of the echo response of a flat plate is half the beam width of an antenna aperture of the same size. The prominent lobe in the horizontal pattern at 68° is a surface traveling-wave lobe closely related to the one appearing at nearly the same angle in the dipole pattern of figure (2.7).

In contrast to the pattern of a flat plate, the RCS pattern of a corner reflector is quite broad. This is true because the corner reflector is a reentrant structure, and no matter what its orientation (within limits, of course), internally reflected waves are directed back toward the source of the incident wave. A corner reflector is formed by two or three flat plates intersecting at right angles, and waves impinging on the first face

estimated by representing the target as a collection of feature, calculating the individual contributions, and then summing the contributions coherently or non-coherently. More detailed formulas are given in section for surface orientations not included.

2.2. Complex Objects

Objects like antennas, insects, birds, airplanes, and ships can be more complex than those discussed above, either because of the multiplicity of scattered on them or because of the complexity of their surface "Electric constants. Insects are examples of the latter.

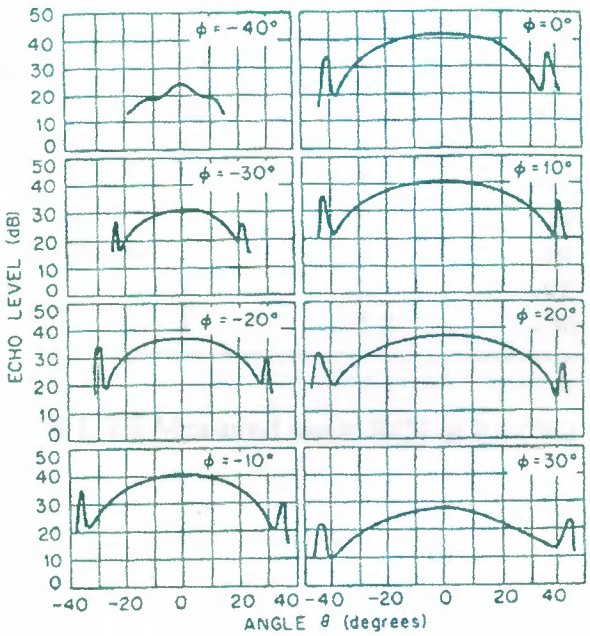

Fig.2.12. RCS pattern of a trihedral corner reflector. Edge of aperture = 24 in; λ = 1.25 cm.

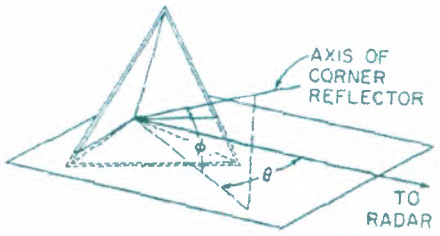

Fig.2.13. Coordinate system for the RCS pattern in fig (2.11).

Measured values for a dozen species are listed in Table (2.2), (The spider is an arachnid, not an insect, of course.). The animals were live for the measurements but had been drugged to immobilize them. figure (2.14) shows the relationship between the RCS and the mass of an insect, with the variation of a water droplet shown for comparison. Similar comparisons have been made for both birds and insects. The following values have been reported for the RCS of a man;

Insect	Length, mm	Width, mm	Broadside RCS, dBsm	End-on RCS, dBsm
Blue-winged locust	20	4	- 30	-40
Armyworm moth	14	4	- 39	-49
Alfalfa caterpillar butterfly	14	1.5	-42	- 57
Honeybee worker	13	6	-40	-45
California harvester ant	13	6	-54	- 57
Range crane fly	13	1	-45	- 57
Green bottle fly	9	3	-46	-50
Twelve-spotted cucumber beetle	8	4	-49	- 53
Convergent lady beetle	5	3	-57	- 60
Spider (unidentified)	5	3.5	- 50	- 52

TABLE 2.2 Measured insect RCS at 9.4 GHz.

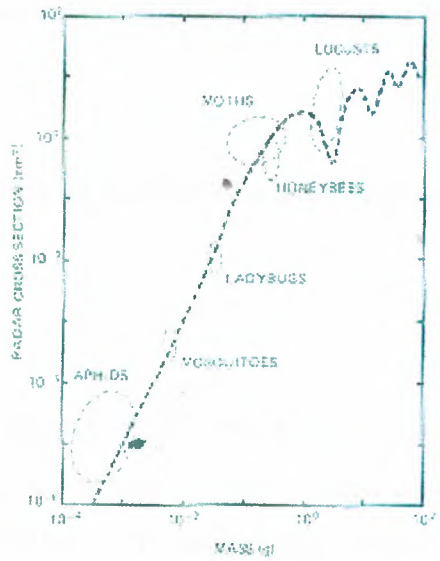

Fig.2.14. Sample of measured RCS of insects are a function of insect mass in 9.4 GHz. The solid trace is the calculated RCS of water droplet for comparison.

Frequency, GHz	RCS, m^2
0.41	0.033-2.33
1.12	0.098-0.997
2.89	0.140-1.05
4.80	0.368-1.88
9.375	0.495-1.22

Examples of the RCS of aircraft are shown in figures (2.14) through (2.16). The B-26 pattern in figure (2.15) was measured at a wavelength of 10 cm (frequency of about 3 GHz); the polar format is useful for display purposes but is not as convenient for detailed comparisons as a rectangular format is. The RCS levels shown in the scale model Boeing 737 patterns of figure (2.15) are those at the measurement frequency. To obtain the corresponding full-scale values, one must add 23.5 dB (10 log 225); the full-scale frequency is one-fifteenth of the measurement frequency in this case, or 667 MHz. The patterns shown in figure (2.16) are medians of RCS averages taken in cells 10° square. With modern data-collecting and -recording equipment, it is feasible to plot measured results at much finer intervals than are plotted in this figure. Note that the data is relative to 1 ft; to convert the displayed results to dBsm, one must subtract 10.3 dB ($10 \log 10.76\ ft^2 / m^2$).

An empirical formula for the RCS of a naval ship is,

$$\sigma = 52 f^{1/2} D^{3/2} \quad , \tag{2.4}$$

where f is the radar frequency is gigahertz and D is the full-load displacement of the vessel in kilotons. The relationship is based on measurements of several ships at low grazing angels and represents the average of the median RCS in the port and starboard bow, and quarter aspects, but excluding the broadside peaks. The statistics include data collected at normal wavelength of 3.25, 10.7 and 23cm for ship displacement ranging from 2 to 17 kilo-tones.

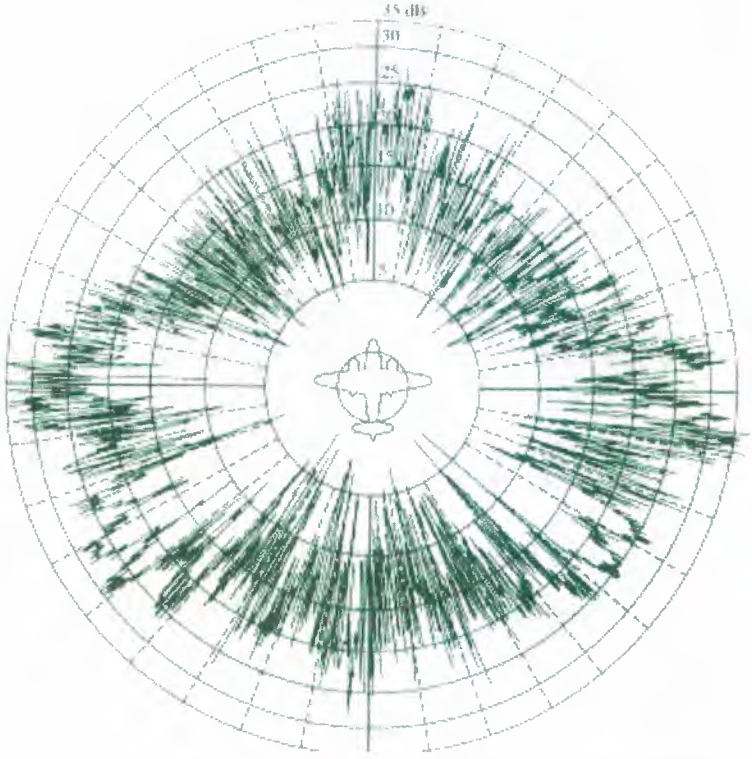

Fig.2.15. charts the RCS of a ship measured at 2.8 and 9.225 GHz at horizontal polarization. The data was collection by a shore-based radar instrumental complex as the ship steamed in a large circle on Chesapeake Bay. The three traces in these charts are 80, 50, 20 percentile levels of the signals collected over aspect angle "windows" 2^{o} wide. The patterns are not symmetrical, especially at higher frequency. Note that the RCS can exceed 1 mi^2 (64.1 dBm).

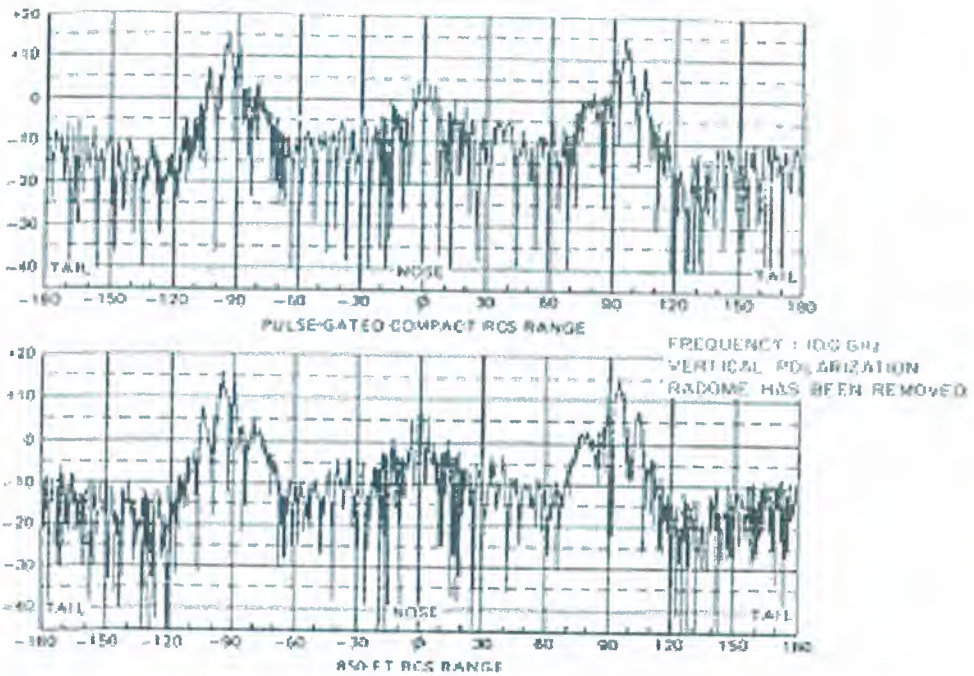

Fig.2.16. Measure of RCS of a one-fifteenth scale model Boeing 737 commercial jet at 10 GHz and vertical polarization

Figure (2.19) summarizes the general RCS levels of the wide variety of targets discussed in this section, with the RCS metallic sphere shown as a function of its volume for comparison. The ordinate is the RCS levels of the wide variety of targets discussed in this section, with the RCS of the metallic sphere shown as a function of its volume for comparison. The ordinate is the RCS in square meters, and the abscissa is the volume of the target in cubic feet. Because the chart is intended only to display the wide range in RCS that may be encountered in practice, the locations of target on the chart are approximately at best. Within given classes of target the RCS may be expected to vary by as much as 20 or 30 dB, depending on frequency, aspect angle, and specific target characteristics.

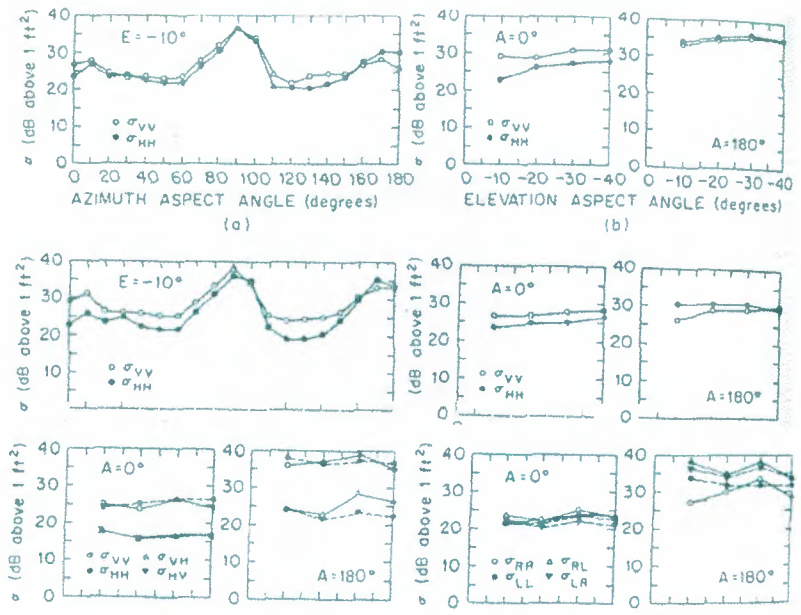

Fig.2.17. Measured RCS of a C-54 aircraft in azimuth and elevation planes for linear and circular polarizations. Plotted values are the average RCS in a cell 10° in azimuth by 10° in elevation. Azimuth patterns a and c are for a fixed elevation angle of -10°. The remaining patterns are in the elevation plane for fixed nose-on or tail-on azimuths. The first and second subscripts give transmitted and received polarizations; *H* and *V* indicate horizontal and vertical polarizations, and *R* and *L* indicate right circular and left circular polarizations.

2.3. RCS Prediction Techniques

Although the complexity and size of most scattering objects preclude the application of exact methods of radar cross-section prediction, exact solutions for simple bodies provide valuable checks for approximate methods. The exact methods are restricted to relatively simple or relatively small objects in the Raleigh and resonant regions, while most of the approximate methods have been developed for the optics region. There are exceptions to these general limitations, of course, the exact solutions for many objects can be used for large bodies in the optics region if one uses arithmetic of sufficient precision, and many of the optics approximations can be extended to bodies of modest electrical size in the resonance region. Low-frequency approximations developed for the Raleigh region can extend into the resonance region.

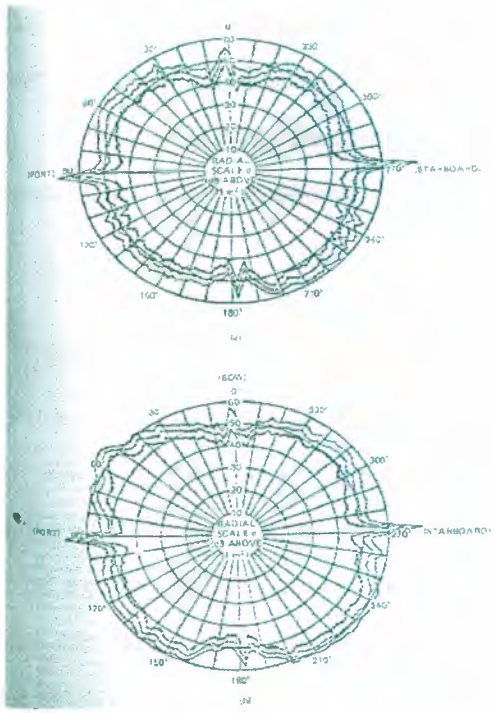

Fig.2.18. Measure RCS of a large naval auxiliary ship for horizontal incident polarization. Upper pattern (a) is for 2.8 GHz and the lower (b) for 9.225 GHz.

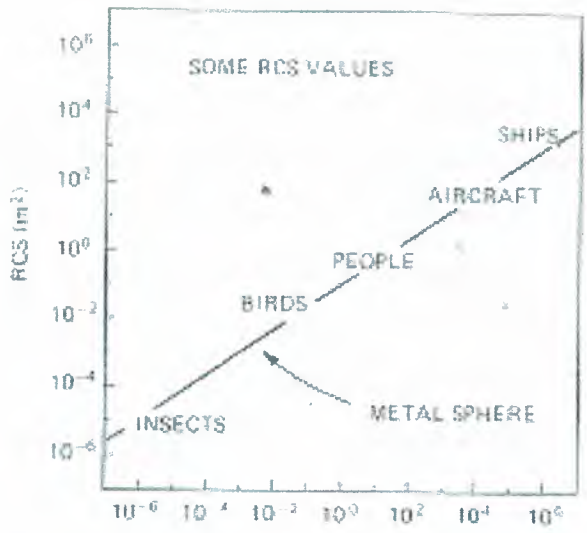

Fig.2.19. Summary of RCS of targets discussed in the section.

2.3.1. Exact Methods

Differential equations. The exact methods are based on either the integral or differential forms of Maxwell's four differential equations constitute a succinct statement of the relationship between electric and magnetic fields produced by currents and charges and by each other. The Fourier equations may be manipulated for isotropic source-free regions to generate the wave equations

$$\nabla^2 F + k^2 F = 0 \quad , \tag{2.5}$$

where F represents either the electric field or the magnetic field. Equation 2.5. is a second order differential which may be solved as a boundary value problem when the fields on the surface of the scattering obstacle are specified. The fields are typically represented as the sum of known and unknown components (incident and scattered fields), and the boundary conditions are known relationship that must be satisfied between the fields (both electric and magnetic) just inside and just outside the surface of the obstacle exposed to the incident wave. Those boundary conditions are particularly simple for solid conducting or dielectric objects.

The boundary conditions involve all three components of the vector fields, and the surface of the body must coincide with a coordinate of the geometrical system in which the body is described. The solution of the wave equation is most useful for those system in which the equation is separable into ordinary differential equations in each of the variables. The scattered fields are typically expressed in terms of infinite series, the coefficients of which are to be determined in the actual solution of the problem. The solution allows the field to be calculated at any point in space, which in RCS problems is the limit as the distance from the obstacle becomes infinite. The product implied in equations (2.1) and (2.2) is then formed from the solution of the wave equation, yielding the scattering cross section or the scattering width.

An example of a solution of the wave equation is the following infinite series for a perfectly conducting sphere:

$$\frac{\sigma}{\pi a^2} = \left| \sum_{n=1}^{\infty} \frac{(-1)^n (2n+1)}{f_n(ka)\left[kaf_{n-1}(ka) - nf_n(ka)\right]} \right|^2 , \qquad (2.6)$$

The function $f_n(x)$ is a combination of spherical Bessel functions of order n and may be formed from the two immediately lower order functions by means of the recursion relationship

$$f_n(x) = \frac{2n-1}{x} f_{n-1}(x) - f_{n-2}(x) , \qquad (2.6)$$

An efficient computational algorithm may be developed by using the two lowest orders as starting values,

$$f_o(x) = 1$$

$$f_1(x) = (1/x) - i$$

Equation (2.6) was used to compute the RCS characteristics plotted in Figs. 2.2 and 2.3. The infinite summation is truncated at the point where additional terms are negligible. The number of terms N required to compute the value of the bracketed term in equation (2.6) to six decimal places for $ka < 100$ is approximately

$$N = 8.53 + 1.21(ka) - 0.001(ka)^2$$

The constants in Equations (2.8) are slightly different for $ka > 100$ and are lower in value for fewer decimal places in the required accuracy.

The solution of the wave equation for the infinite, perfectly conducting circular cylinder can be resolved into two cases, one each for the incident electric or magnetic field parallel to the cylinder axis. The expressions are slightly simpler than Equation (2.6) and involve cylindrical Bessel functions of the first and second kinds. Figure (2.20) and (2.21) illustrates the backscattering behavior for the two principal polarizations as a function of the electrical circumference of the cylinder.

The response for E polarization figure (2.20) is much larger than geometric optics value, πa when the cylinder is less than a fraction of a wavelength in circumference but it approaches the geometric optics value within a few percent for cylinders larger than about 2 wavelengths in circumference. The backscattering is markedly different for *H* polarization figure (2.21), exhibiting the same kind of undulations noted earlier in the case of the metallic sphere. These undulations are caused by creeping waves that propagate around the rear of the cylinder just as they do around a sphere. However, the peaks and nulls of the sphere and cylinder interference patterns are not perfectly aligned with each another, suggesting that are the relative angles between the creeping waves and specular contributions are slightly different for the two geometries.

The exact expression for the RCS of the dielectric cylinder is more complicated than for the conducting cylinder, but it accounts for the fact that energy penetrates the interior of the body. Unless the cylinder material is a
Perfect insulator,

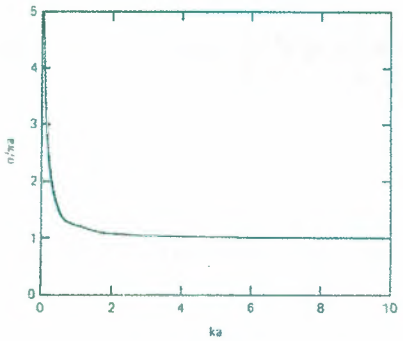

Fig 2.20 Normalized scattering width of an infinite, perfectly conducting cylinder for E polarization (incident electric field parallel to the cylinder axis). The normalization is with respect to the geometric optics return from the cylinder.

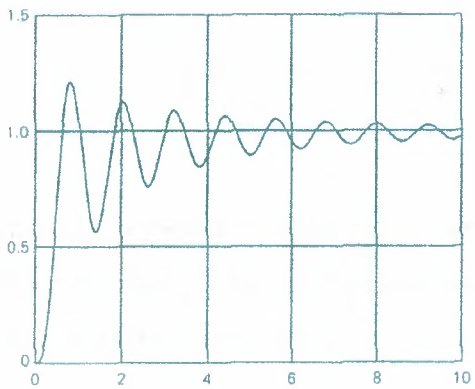

Fig.2.21. Normalized scattering width of an infinite, perfectly conducting cylinder of H polarization (incident magnetic field parallel to the cylinder axis)

Its index of refraction is a complex function whose imaginary part gives rise to losses in the material. This in turn requires the computation of Bess functions of complex argument, not an insignificant undertaking. Quite simple formulas for the scattering width may be obtained in the Raleigh region, however, for which the cylinder diameter is much smaller than the incident wavelength. Figure (2.5) illustrates the scattering behavior of very thin dielectric cylinders.

2.3.1.1. Integral Equations

Maxwell's equations may also be manipulated to generate a pair of integral equations(known as Stratton-Chu equation's).

$$\vec{E}_S = \oint \left\{ ikZ_o \left(n \times \vec{H} \right) \psi + \left(n \times \vec{E} \right) \times \nabla \psi + \left(n \cdot \vec{E} \right) \nabla \psi \right\} \vec{ds} \ , \qquad (2.9)$$

$$\vec{H}_S = \oint \left\{ ikZ_O \left(n \times \vec{H} \right) \psi + \left(n \times H \right) \times \nabla \psi + \left(n \cdot H \right) \nabla \psi \right\} \vec{ds} \ , \qquad (2.10)$$

where $\hat{n}$ is the unit surface normal erected at the surface patch dS and the Green's function ψ is,

$$\psi = e^{ikr} / 4\pi r \ , \qquad (2.11)$$

the distance r in Equation (2.11) is measured from the surface patch dS to the point at which the scattered fields are desired. These expressions state that if the total electric field and magnetic field distributions are known over a closed surface S, the scattered

field any where in the space can be compared by summing (integrating) those surface field distributions.

The surface field distributions may be interpreted as induced electric and magnetic currents and charges, which become unknowns to be determined in a solution. The two equations are coupled because the unknown appear in both. Unknown quantities also appear in both sides of the equations because the induced fields include the unknown field scattered intensity. The method of solution is know as **method of moments (MOM),** reducing the integral equation to a collection of homogeneous linear equation which may be solved by matrix techniques.

The solutions of integral equations begin with the specifications of the relation between the incident and scattered fields on the surface S, as governed by the material of which the object is made. If the body is a perfect conductor or if the electric and magnetic fields can be related by a constant (the surface impedance boundary conditions), then equations become decoupled, only one or the other needs to be solved. If the body is not homogeneous then the field must be sampled at intervals within its interior volume, complicating the solution.

Once the boundary conditions have been specified, the surface S is split into a collection of small discrete patches, as suggested in figure (2.22). The patches must be small enough (typically less than 0.2λ) that the unknown current and charges on each patch are constant or one can be described as simple function. A weighing function may be assigned to each patch, and the problem is essentially solved when the amplitude and the phase of those functions have been determined.

The point of observation is forced down to a general surface patch, whereupon the fields on the left-hand side of equation (2.9) and (2.10) are those due to the fields on all coupling patches, plus the incident field and "self-field". The self-field (or charge or current) is moved to the right side of the equations, leaving only the known incident field on the left side. When the process is repeated for each patch on the surface, a system of $2n$ linear homogeneous equations in $2n$ unknown is generated. If the

boundary conditions permit the decoupling of the equations, the number of unknown may be halved (n equations in n unknowns). The coefficients of the resulting matrix involve only the electrical distance (in wavelengths) between all patches taken by pairs and the orientations of the patch surface normal. The unknown fields may be found by inverting the resulting matrix and multiplying the inverted matrix by the column matrix representing the incident at each field at each patch. The surface fields are then summed in integrals like equations (2.9) and (2.10) to obtain the scattered field, which may be inserted in equation (2.11) to compute the RCS, Equation (2.2) and the two-dimensional counterparts of equations (2.9) and (2.10) must be used for two-dimensional geometries, of course.

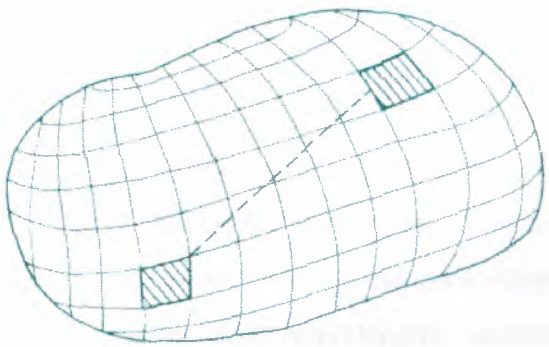

Fig.2.22 The method of moments divides the body surface into a collection of discrete patches.

The method of moments has become a powerful tool in the prediction and analysis of electromagnetic scattering, with applications in antenna design as well as RCS prediction. The method has three limitations, however,

First, because computer memory and processing time both increase rapidly with the electrical size of the object, MOM is economically restricted to objects not much more than a few wavelengths, or perhaps a few dozen wavelengths, in size. As such, MOM is not a useful tool for predicting the RCS of, say, a jet fighter in the beam of radar operating at 10 GHz. The second limitation is that MOM yields numbers, not formulas, and is therefore a numerical experimental tool. Trends may be established only by running a numerical experiment repeatedly for small parametric changes in the geometry or configuration of an object or in the angle of arrival or the frequency of the

incident wave. Third, the solutions for some objects may contain spurious resonances that do not actually exist, thereby reducing the confidence one may have in applying the method to arbitrary structures.

Figure (2.23) traces the broadside RCS of a perfectly conducting cube computed by means of the method of moments. Spurious resonances were suppressed in the computations by forcing the normal surface component of the magnetic field to zero. The surface of the cube was divided into 384 patches (64 patches per face), which was about the limit of the central memory of the cyber 750 computer used in the computations. It required more than 2 h for the cyber 750 to generate the data plotted in the figure (2.26).

2.3.2. Approximate Methods

Approximate methods for computing scattered fields are available in both the Raleigh and the optics regions. Raleigh region approximations may be derived by expanding the wave equation (2.5) power series of the wave number k. The expansion is quasi-static for small wave number (long wavelengths compared with typical body dimensions), a higher order terms become progressively more difficult to obtain. The K pattern of a Raleigh scatterer is very broad, especially if the object has similar transverse and longitudinal dimensions. The magnitude of the echo proportional to the square of the volume of the object and varies as to the power of the frequency of the incident wave. Because the method of moments is well suited to the solution of the Raleigh region problems, approximate methods for predicting the RCS of electrically small objects are not represented here.

Several approximate methods have been devised for the optics region, each with its particular advantages and illuminations. The most mature of the methods are geometric optics and physical optics, with latter methods attacking the problems of diffraction from edges and shadow boundaries. While the general accuracy of the optic region approximations improves as the scattering obstacles become electrically large, some of them give reasonable accurate results (within 1 or 2 dB) for objects as small as wavelength or so.

estimated by representing the target as a collection of feature, calculating the individual contributions, and then summing the contributions coherently or non-coherently. More detailed formulas are given in section for surface orientations not included.

2.2. Complex Objects

Objects like antennas, insects, birds, airplanes, and ships can be more complex than those discussed above, either because of the multiplicity of scattered on them or because of the complexity of their surface "Electric constants. Insects are examples of the latter.

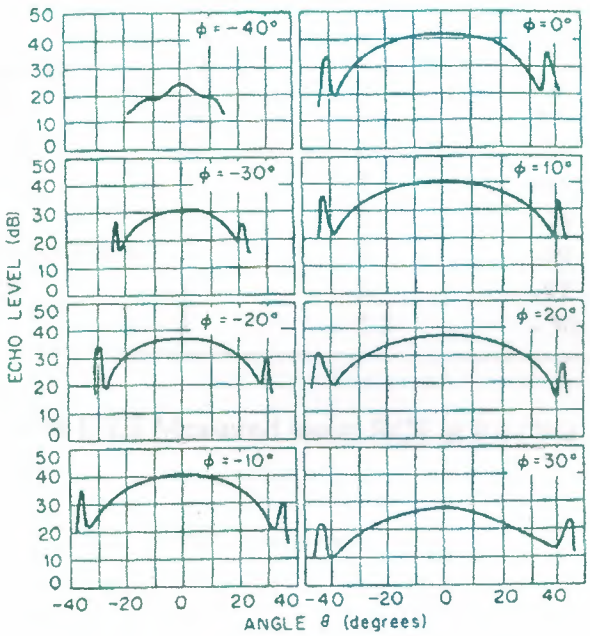

Fig.2.12. RCS pattern of a trihedral corner reflector. Edge of aperture = 24 in; λ = 1.25 cm.

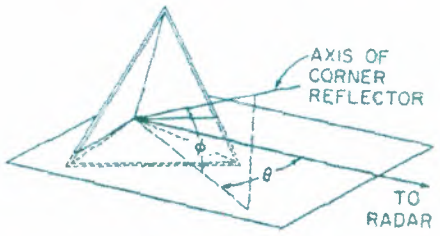

Fig.2.13. Coordinate system for the RCS pattern in fig (2.11).

Measured values for a dozen species are listed in Table (2.2), (The spider is an arachnid, not an insect, of course.). The animals were live for the measurements but had been drugged to immobilize them. figure (2.14) shows the relationship between the RCS and the mass of an insect, with the variation of a water droplet shown for comparison. Similar comparisons have been made for both birds and insects. The following values have been reported for the RCS of a man;

Insect	Length, mm	Width, mm	Broadside RCS, dBsm	End-on RCS, dBsm
Blue-winged locust	20	4	- 30	-40
Armyworm moth	14	4	- 39	-49
Alfalfa caterpillar butterfly	14	1.5	-42	- 57
Honeybee worker	13	6	-40	-45
California harvester ant	13	6	-54	- 57
Range crane fly	13	1	-45	- 57
Green bottle fly	9	3	-46	-50
Twelve-spotted cucumber beetle	8	4	-49	- 53
Convergent lady beetle	5	3	-57	- 60
Spider (unidentified)	5	3.5	- 50	- 52

TABLE 2.2 Measured insect RCS at 9.4 GHz.

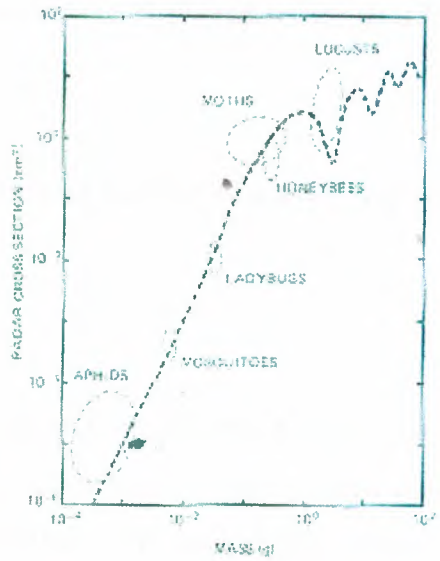

Fig.2.14. Sample of measured RCS of insects are a function of insect mass in 9.4 GHz. The solid trace is the calculated RCS of water droplet for comparison.

Frequency, GHz	RCS, m^2
0.41	0.033-2.33
1.12	0.098-0.997
2.89	0.140-1.05
4.80	0.368-1.88
9.375	0.495-1.22

Examples of the RCS of aircraft are shown in figures (2.14) through (2.16). The B-26 pattern in figure (2.15) was measured at a wavelength of 10 cm (frequency of about 3 GHz); the polar format is useful for display purposes but is not as convenient for detailed comparisons as a rectangular format is. The RCS levels shown in the scale model Boeing 737 patterns of figure (2.15) are those at the measurement frequency. To obtain the corresponding full-scale values, one must add 23.5 dB (10 log 225); the full-scale frequency is one-fifteenth of the measurement frequency in this case, or 667 MHz. The patterns shown in figure (2.16) are medians of RCS averages taken in cells 10° square. With modern data-collecting and -recording equipment, it is feasible to plot measured results at much finer intervals than are plotted in this figure. Note that the data is relative to 1 ft; to convert the displayed results to dBsm, one must subtract 10.3 dB ($10 \log 10.76\ ft^2 / m^2$).

An empirical formula for the RCS of a naval ship is,

$$\sigma = 52 f^{1/2} D^{3/2} \quad , \tag{2.4}$$

where f is the radar frequency is gigahertz and D is the full-load displacement of the vessel in kilotons. The relationship is based on measurements of several ships at low grazing angels and represents the average of the median RCS in the port and starboard bow, and quarter aspects, but excluding the broadside peaks. The statistics include data collected at normal wavelength of 3.25, 10.7 and 23cm for ship displacement ranging from 2 to 17 kilo-tones.

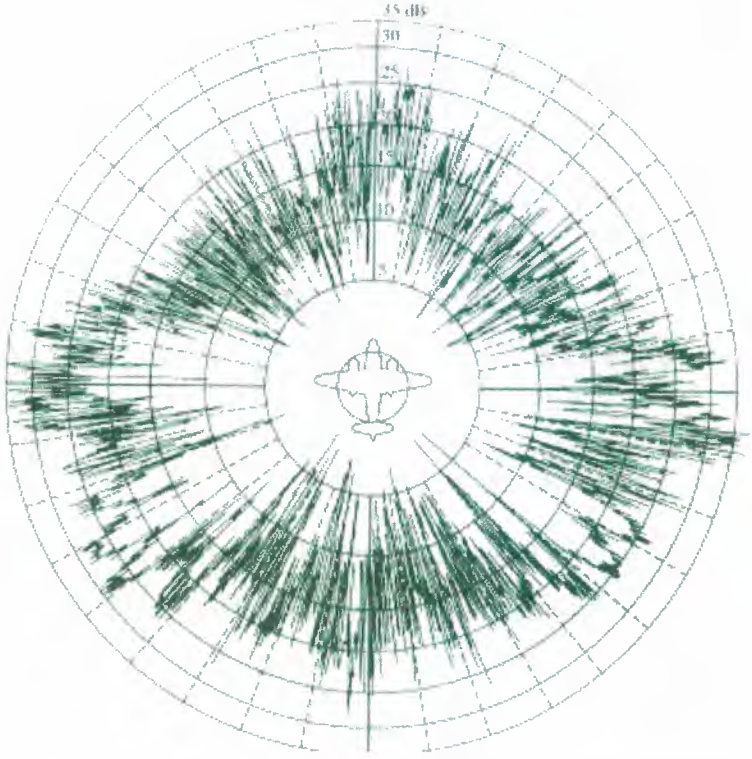

Fig.2.15. charts the RCS of a ship measured at 2.8 and 9.225 GHz at horizontal polarization. The data was collection by a shore-based radar instrumental complex as the ship steamed in a large circle on Chesapeake Bay. The three traces in these charts are 80, 50, 20 percentile levels of the signals collected over aspect angle "windows" 2^{o} wide. The patterns are not symmetrical, especially at higher frequency. Note that the RCS can exceed 1 mi^2 (64.1 dBm).

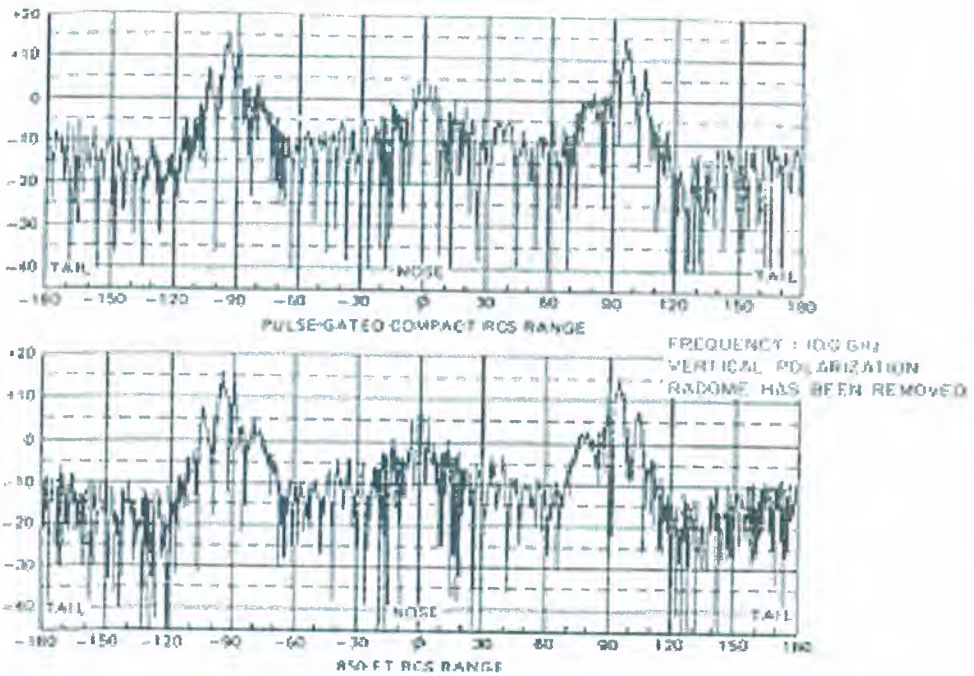

Fig.2.16. Measure of RCS of a one-fifteenth scale model Boeing 737 commercial jet at 10 GHz and vertical polarization

Figure (2.19) summarizes the general RCS levels of the wide variety of targets discussed in this section, with the RCS metallic sphere shown as a function of its volume for comparison. The ordinate is the RCS levels of the wide variety of targets discussed in this section, with the RCS of the metallic sphere shown as a function of its volume for comparison. The ordinate is the RCS in square meters, and the abscissa is the volume of the target in cubic feet. Because the chart is intended only to display the wide range in RCS that may be encountered in practice, the locations of target on the chart are approximately at best. Within given classes of target the RCS may be expected to vary by as much as 20 or 30 dB, depending on frequency, aspect angle, and specific target characteristics.

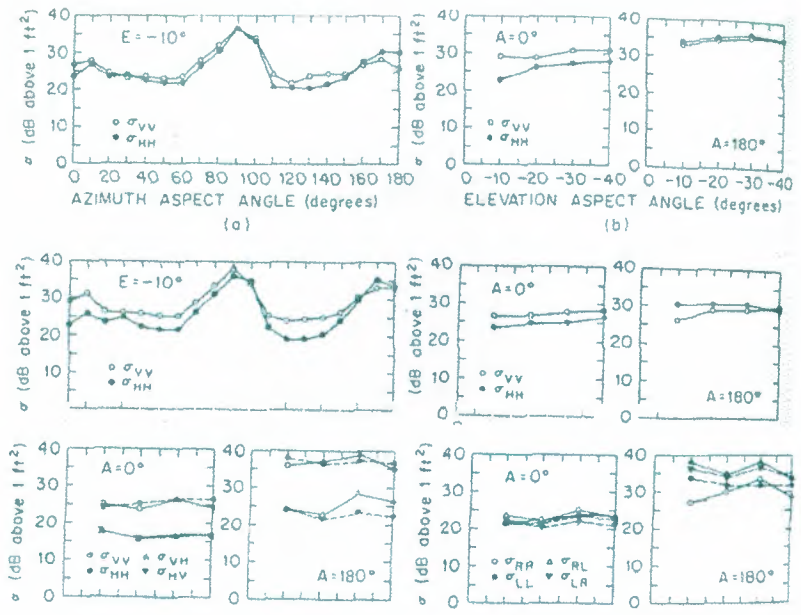

Fig.2.17. Measured RCS of a C-54 aircraft in azimuth and elevation planes for linear and circular polarizations. Plotted values are the average RCS in a cell 10° in azimuth by 10° in elevation. Azimuth patterns a and c are for a fixed elevation angle of -10°. The remaining patterns are in the elevation plane for fixed nose-on or tail-on azimuths. The first and second subscripts give transmitted and received polarizations; *H* and *V* indicate horizontal and vertical polarizations, and *R* and *L* indicate right circular and left circular polarizations.

2.3. RCS Prediction Techniques

Although the complexity and size of most scattering objects preclude the application of exact methods of radar cross-section prediction, exact solutions for simple bodies provide valuable checks for approximate methods. The exact methods are restricted to relatively simple or relatively small objects in the Raleigh and resonant regions, while most of the approximate methods have been developed for the optics region. There are exceptions to these general limitations, of course, the exact solutions for many objects can be used for large bodies in the optics region if one uses arithmetic of sufficient precision, and many of the optics approximations can be extended to bodies of modest electrical size in the resonance region. Low-frequency approximations developed for the Raleigh region can extend into the resonance region.

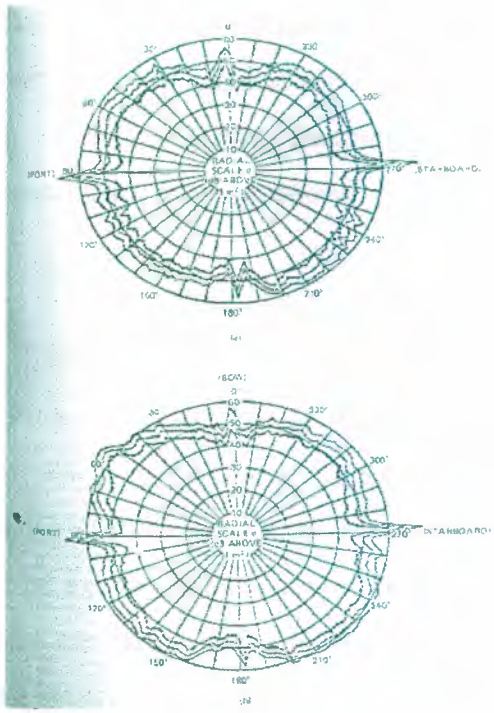

Fig.2.18. Measure RCS of a large naval auxiliary ship for horizontal incident polarization. Upper pattern (a) is for 2.8 GHz and the lower (b) for 9.225 GHz.

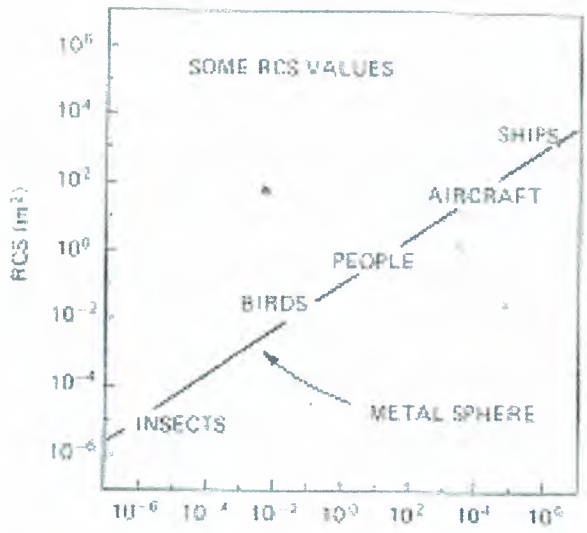

Fig.2.19. Summary of RCS of targets discussed in the section.

2.3.1. Exact Methods

Differential equations. The exact methods are based on either the integral or differential forms of Maxwell's four differential equations constitute a succinct statement of the relationship between electric and magnetic fields produced by currents and charges and by each other. The Fourier equations may be manipulated for isotropic source-free regions to generate the wave equations

$$\nabla^2 F + k^2 F = 0 \quad , \tag{2.5}$$

where F represents either the electric field or the magnetic field. Equation 2.5. is a second order differential which may be solved as a boundary value problem when the fields on the surface of the scattering obstacle are specified. The fields are typically represented as the sum of known and unknown components (incident and scattered fields), and the boundary conditions are known relationship that must be satisfied between the fields (both electric and magnetic) just inside and just outside the surface of the obstacle exposed to the incident wave. Those boundary conditions are particularly simple for solid conducting or dielectric objects.

The boundary conditions involve all three components of the vector fields, and the surface of the body must coincide with a coordinate of the geometrical system in which the body is described. The solution of the wave equation is most useful for those system in which the equation is separable into ordinary differential equations in each of the variables. The scattered fields are typically expressed in terms of infinite series, the coefficients of which are to be determined in the actual solution of the problem. The solution allows the field to be calculated at any point in space, which in RCS problems is the limit as the distance from the obstacle becomes infinite. The product implied in equations (2.1) and (2.2) is then formed from the solution of the wave equation, yielding the scattering cross section or the scattering width.

An example of a solution of the wave equation is the following infinite series for a perfectly conducting sphere:

$$\frac{\sigma}{\pi a^2} = \left| \sum_{n=1}^{\infty} \frac{(-1)^n (2n+1)}{f_n(ka)\left[kaf_{n-1}(ka) - nf_n(ka)\right]} \right|^2 , \qquad (2.6)$$

The function $f_n(x)$ is a combination of spherical Bessel functions of order n and may be formed from the two immediately lower order functions by means of the recursion relationship

$$f_n(x) = \frac{2n-1}{x} f_{n-1}(x) - f_{n-2}(x) , \qquad (2.6)$$

An efficient computational algorithm may be developed by using the two lowest orders as starting values,

$$f_o(x) = 1$$

$$f_1(x) = (1/x) - i$$

Equation (2.6) was used to compute the RCS characteristics plotted in Figs. 2.2 and 2.3. The infinite summation is truncated at the point where additional terms are negligible. The number of terms N required to compute the value of the bracketed term in equation (2.6) to six decimal places for $ka < 100$ is approximately

$$N = 8.53 + 1.21(ka) - 0.001(ka)^2$$

The constants in Equations (2.8) are slightly different for $ka > 100$ and are lower in value for fewer decimal places in the required accuracy.

The solution of the wave equation for the infinite, perfectly conducting circular cylinder can be resolved into two cases, one each for the incident electric or magnetic field parallel to the cylinder axis. The expressions are slightly simpler than Equation (2.6) and involve cylindrical Bessel functions of the first and second kinds. Figure (2.20) and (2.21) illustrates the backscattering behavior for the two principal polarizations as a function of the electrical circumference of the cylinder.

The response for E polarization figure (2.20) is much larger than geometric optics value, πa when the cylinder is less than a fraction of a wavelength in circumference but it approaches the geometric optics value within a few percent for cylinders larger than about 2 wavelengths in circumference. The backscattering is markedly different for *H* polarization figure (2.21), exhibiting the same kind of undulations noted earlier in the case of the metallic sphere. These undulations are caused by creeping waves that propagate around the rear of the cylinder just as they do around a sphere. However, the peaks and nulls of the sphere and cylinder interference patterns are not perfectly aligned with each another, suggesting that are the relative angles between the creeping waves and specular contributions are slightly different for the two geometries.

The exact expression for the RCS of the dielectric cylinder is more complicated than for the conducting cylinder, but it accounts for the fact that energy penetrates the interior of the body. Unless the cylinder material is a
Perfect insulator,

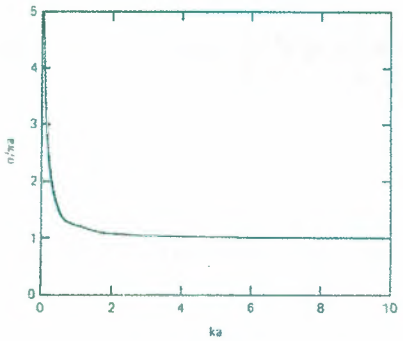

Fig 2.20 Normalized scattering width of an infinite, perfectly conducting cylinder for E polarization (incident electric field parallel to the cylinder axis). The normalization is with respect to the geometric optics return from the cylinder.

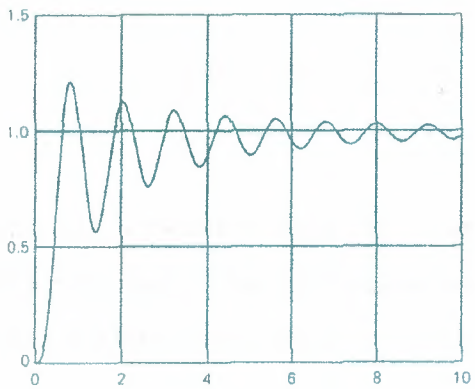

Fig.2.21. Normalized scattering width of an infinite, perfectly conducting cylinder of H polarization (incident magnetic field parallel to the cylinder axis)

Its index of refraction is a complex function whose imaginary part gives rise to losses in the material. This in turn requires the computation of Bess functions of complex argument, not an insignificant undertaking. Quite simple formulas for the scattering width may be obtained in the Raleigh region, however, for which the cylinder diameter is much smaller than the incident wavelength. Figure (2.5) illustrates the scattering behavior of very thin dielectric cylinders.

2.3.1.1. Integral Equations

Maxwell's equations may also be manipulated to generate a pair of integral equations(known as Stratton-Chu equation's).

$$\vec{E}_S = \oint \left\{ ikZ_o \left(n \times \vec{H} \right) \psi + \left(n \times \vec{E} \right) \times \nabla \psi + \left(n \cdot \vec{E} \right) \nabla \psi \right\} \vec{ds} \ , \qquad (2.9)$$

$$\vec{H}_S = \oint \left\{ ikZ_O \left(n \times \vec{H} \right) \psi + \left(n \times H \right) \times \nabla \psi + \left(n \cdot H \right) \nabla \psi \right\} \vec{ds} \ , \qquad (2.10)$$

where $\hat{n}$ is the unit surface normal erected at the surface patch dS and the Green's function ψ is,

$$\psi = e^{ikr} / 4\pi r \ , \qquad (2.11)$$

the distance r in Equation (2.11) is measured from the surface patch dS to the point at which the scattered fields are desired. These expressions state that if the total electric field and magnetic field distributions are known over a closed surface S, the scattered

field any where in the space can be compared by summing (integrating) those surface field distributions.

The surface field distributions may be interpreted as induced electric and magnetic currents and charges, which become unknowns to be determined in a solution. The two equations are coupled because the unknown appear in both. Unknown quantities also appear in both sides of the equations because the induced fields include the unknown field scattered intensity. The method of solution is know as **method of moments (MOM),** reducing the integral equation to a collection of homogeneous linear equation which may be solved by matrix techniques.

The solutions of integral equations begin with the specifications of the relation between the incident and scattered fields on the surface S, as governed by the material of which the object is made. If the body is a perfect conductor or if the electric and magnetic fields can be related by a constant (the surface impedance boundary conditions), then equations become decoupled, only one or the other needs to be solved. If the body is not homogeneous then the field must be sampled at intervals within its interior volume, complicating the solution.

Once the boundary conditions have been specified, the surface S is split into a collection of small discrete patches, as suggested in figure (2.22). The patches must be small enough (typically less than 0.2λ) that the unknown current and charges on each patch are constant or one can be described as simple function. A weighing function may be assigned to each patch, and the problem is essentially solved when the amplitude and the phase of those functions have been determined.

The point of observation is forced down to a general surface patch, whereupon the fields on the left-hand side of equation (2.9) and (2.10) are those due to the fields on all coupling patches, plus the incident field and "self-field". The self-field (or charge or current) is moved to the right side of the equations, leaving only the known incident field on the left side. When the process is repeated for each patch on the surface, a system of $2n$ linear homogeneous equations in $2n$ unknown is generated. If the

boundary conditions permit the decoupling of the equations, the number of unknown may be halved (n equations in n unknowns). The coefficients of the resulting matrix involve only the electrical distance (in wavelengths) between all patches taken by pairs and the orientations of the patch surface normal. The unknown fields may be found by inverting the resulting matrix and multiplying the inverted matrix by the column matrix representing the incident at each field at each patch. The surface fields are then summed in integrals like equations (2.9) and (2.10) to obtain the scattered field, which may be inserted in equation (2.11) to compute the RCS, Equation (2.2) and the two-dimensional counterparts of equations (2.9) and (2.10) must be used for two-dimensional geometries, of course.

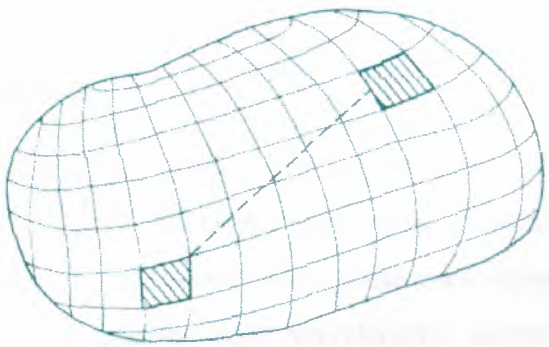

Fig.2.22 The method of moments divides the body surface into a collection of discrete patches.

The method of moments has become a powerful tool in the prediction and analysis of electromagnetic scattering, with applications in antenna design as well as RCS prediction. The method has three limitations, however,

First, because computer memory and processing time both increase rapidly with the electrical size of the object, MOM is economically restricted to objects not much more than a few wavelengths, or perhaps a few dozen wavelengths, in size. As such, MOM is not a useful tool for predicting the RCS of, say, a jet fighter in the beam of radar operating at 10 GHz. The second limitation is that MOM yields numbers, not formulas, and is therefore a numerical experimental tool. Trends may be established only by running a numerical experiment repeatedly for small parametric changes in the geometry or configuration of an object or in the angle of arrival or the frequency of the

incident wave. Third, the solutions for some objects may contain spurious resonances that do not actually exist, thereby reducing the confidence one may have in applying the method to arbitrary structures.

Figure (2.23) traces the broadside RCS of a perfectly conducting cube computed by means of the method of moments. Spurious resonances were suppressed in the computations by forcing the normal surface component of the magnetic field to zero. The surface of the cube was divided into 384 patches (64 patches per face), which was about the limit of the central memory of the cyber 750 computer used in the computations. It required more than 2 h for the cyber 750 to generate the data plotted in the figure (2.26).

2.3.2. Approximate Methods

Approximate methods for computing scattered fields are available in both the Raleigh and the optics regions. Raleigh region approximations may be derived by expanding the wave equation (2.5) power series of the wave number k. The expansion is quasi-static for small wave number (long wavelengths compared with typical body dimensions), a higher order terms become progressively more difficult to obtain. The K pattern of a Raleigh scatterer is very broad, especially if the object has similar transverse and longitudinal dimensions. The magnitude of the echo proportional to the square of the volume of the object and varies as to the power of the frequency of the incident wave. Because the method of moments is well suited to the solution of the Raleigh region problems, approximate methods for predicting the RCS of electrically small objects are not represented here.

Several approximate methods have been devised for the optics region, each with its particular advantages and illuminations. The most mature of the methods are geometric optics and physical optics, with latter methods attacking the problems of diffraction from edges and shadow boundaries. While the general accuracy of the optic region approximations improves as the scattering obstacles become electrically large, some of them give reasonable accurate results (within 1 or 2 dB) for objects as small as wavelength or so.

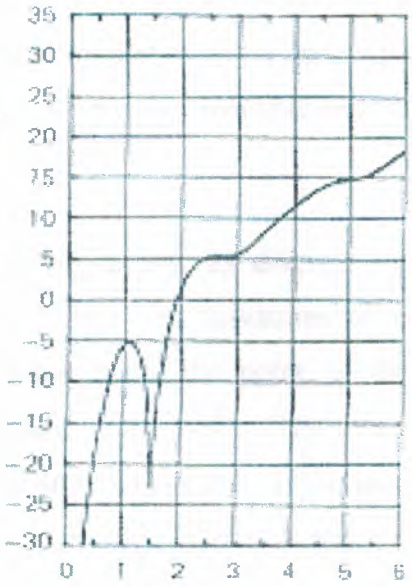

Fig.2.23. Broadside RCS of a perfectly conducting cube.

The theory of the geometric optics is based on the conversation of energy within a slender fictious tube called a ray. The direction of propagation is along the tube, the contours of equal phase are perpendicular to it. In a lossless medium, all the energy entering a tube must come out the other, but the energy lossless within the medium may also be accounted for. An incident wave may be represented as a collection of a large number of rays, and when a ray strikes the face, part of energy is reflected and part of it is absorbed by the surface. The amplitude and the phase of the reflected and transmitted rays depend on the properties of the media on either side of the surface. The reflection is perfect if the material is perfectly conducting, and no energy is transmitted across the boundary. When the energy can pass through the surface, transmitted rays are bent towards the surface normal in crossing a surface into an electrically denser medium (higher index of refraction) and away from the surface normal into a less denser medium. The bending of rays is known as refraction.

Depending upon surface of curvature and body material, reflected and transmitted waves may be diverged from one another or they may converge towards each other. This dependence is the basis of the design of lenses at radar wavelength as well as optical wavelength. The variation of the refractive index of water molecules with

wavelength is responsible for rainbow phenomenon, the result of the two refractions near the front of the spherical droplet of water and single internal reflection from rear. Secondary and tertiary rainbows are due to double and triple internal reflections.

The reduction in intensity as the ray diverges (spread way) from the point of reflection can be calculated from the curvatures of the reflecting surface and the incident wave at the specular point, the point on the surface where the angle of reflection is equal to the angle of incidence. The principle radii of curvatures of the surface are measured in two orthogonal planes at the specular points, as shown in figure 2.24. When the incident wave is planer and the direction of interest is back towards the source, the geometric optics RCS is simply,

$$\sigma = \pi a_1 a_2 \quad , \tag{2.12}$$

This formula becomes exact in the optical limit of vanishing wavelength and is probably accurate to 10 or 15 percent for radii of curvature as small as 2 or 3 wavelengths. It assumes that the specular point is not close to an edge. When applied to dielectric objects, the expression should be multiplied by the square of the voltage reflection coefficient associated with the material properties of the object. Internal reflections should also be accounted for, and the phase of internally reflected rays adjusted according to the electrical path lengths traversed within the body material. The net RCS then should be computed as the coherent sum of the surface reflection plus all significant internal reflections. Equation (2.12) fails when one or both surface radii of curvature at the specular point become infinite, yielding infinite RCS, which is obviously wrong. This occurs for flat and singly curved surfaces.

The theory of physical optics (PO) is a suitable alternative for bodies with flat and singly curved surface features. The theory is based on two approximations in the application of equations (2.9) and (2.10), both of which are reasonably effective approximations in a host of practical cases. The first is *the far-field approximation,* which assumes that the distance from the scattering obstacle to the point of observation is large compared with any dimension of the obstacle itself. This allows one to replace the gradient of Green's function with

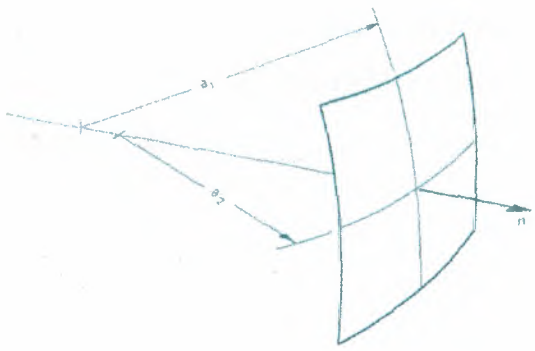

Fig.2.24. The geometric optics RCS of a doubly curved surface depends on the principal radii of curvature at the spectacular points. The specular point is that point on the surface normal points towards the radar.

where a_1 and a_2 are the radii of curvature of the body surface at the specular point.

$$\nabla\psi = ik\psi_o s \quad , \tag{2.13}$$

$$\psi_o = e^{-ikr\cdot s} e^{ikR_o} / 4\pi R_o \quad , \tag{2.14}$$

where r is the position vector of integration patch dS and s is a unit vector pointing from an origin in or near the object to the far-field observation point, usually back toward the radar. Ro is the distance from the origin of the object to the far-field observation point.

The second is the *tangent plane approximation,* in which the tangential field components $n \times E$ and $n \times H$ are approximated by their geometric optics values. That is, a tangent plane is passed through the surface coordinate at the patch dS, and the total surface fields are taken to be precisely those that would have existed had the surface at dS been infinite and perfectly flat. Thus the unknown fields in the integrals of equations (2.9) and (2.10) may be expressed entirely in terms of the known incident field values. The problem then becomes one of evaluating one of the two integrals and substituting the result into equations (2.1) to obtain the RCS.

If the surface is a good conductor, the total tangential electric field is virtually zero and the total tangential magnetic field is twice the amplitude of the incident tangential magnetic field.

$$n \times E = 0 \quad , \tag{2.15}$$

$$n \times H = \{2n \times H_i\} \quad , \quad \text{illuminated surface}$$

$$n \times H = 0 \quad , \quad \text{shaded surface} \tag{2.16}$$

Note that the tangential components of both the electric and the magnetic fields are set to zero over those parts of the surface shaded from the incident field by other body surfaces. Other approximations may be devised for non-conducting surfaces; if the incident wavelength is long enough, for example, the surface of a soap bubble or the leaf of a tree may be modeled as a thin membrane, on which neither the electric nor the magnetic fields are zero.

The integral is easy to evaluate for flat metallic plates because the phase is the only quantity within the integral that varies, and it varies linearly across the surface. The result for a rectangular plate viewed in a *principal plane* is

$$\sigma = 4\pi \left| \frac{A \cos\theta}{\lambda} \bullet \frac{\sin(kl \sin\theta)}{kl \sin\theta} \right|^2 , \tag{2.17}$$

where A is the physical area of the plate, 0 is the angle between its surface normal and the direction to the radar, and t is the length of the plate in the principal plane containing the surface normal and the radar line of sight. A more general physical optics formula is available for the bistatic scattering of a polygonal plate with an arbitrary number of sides.

A rectangular plate has a pair of orthogonal principal planes, and the edge in equation (2.17) is that lying in the plane of measurement. If we designate w as the width of the plate in the opposite plane, the area of the plate is $A = lw$. To evaluate the maximum side lobe levels of the plate RCS in the principal plane of measurement we may replace the numerator of the sin (x)/x term in equation (2.17) by unit. Normalizing with aspect to the square of the width of the plane in the to the measurement plane, we find the maximum side lobe levels to be

$$\frac{\sigma}{w^2} = \frac{1}{\pi \tan^2 \theta} \quad , \tag{2.18}$$

Note that this result is *independent of the radar wavelength.*

The frequency independence of the principal-plane side lobes is illustrated in figure (2.25). For viewing angles away from normal incidence, the plate edges are the dominant sources of echo, and the sin *(x)/x* pattern is the result of the individual edge contributions changing phase with respect to each other as the aspect angle changes. Noting from Table (2.1); that the radar echoes of straight edges perpendicular to the line of sight are independent of frequency, the result of equation (2.18) is to be expected.

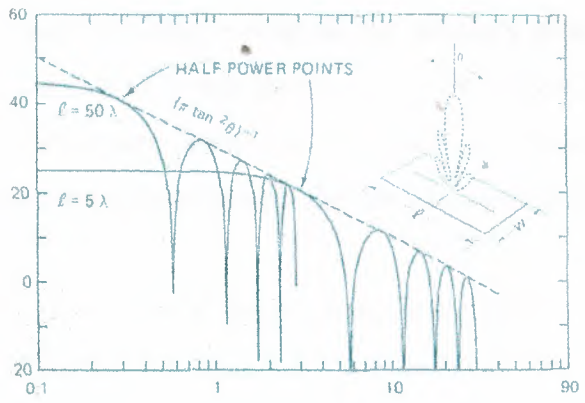

Fig.2.25. The amplitudes of the principle-plane side lobes of RCS of a flat rectangular plates are independent of frequency.

The physical optics formula for the RCS of a circular metallic disk is

$$\sigma = 16\pi \left| \frac{A\cos\theta}{\lambda} \bullet \frac{J_1(kd\sin\theta)}{kd\sin\theta} \right|^2 , \qquad (2.19)$$

where A is the physical area of the disk, d is its diameter, and J1(x) is the Bessel function of the first kind of order 1. Equations (2.17) and (2.19) both reduce to the value listed in Table 2.1 for normal incidence.

The integral is somewhat more complicated to evaluate when the surface is singly or doubly curved. An exact evaluation can be performed for a circular cylinder and a spherical cap viewed along the axis of symmetry, but not for a truncated cone or a spherical cap seen along other than the axis of symmetry- Even so, the exact evaluation for the cylinder includes fictitious contributions from the shadow boundaries at the sides of the cylinder that do not appear in a *stationary phase approximation.*

The amplitude of the elemental surface patch contributions changes slowly over the surface of integration while the phase changes much more rapidly-such, the net contribution in regions of rapid phase change is essentially zero an may be ignored. As the specular regions are approached, on the other hand, phase variation slows down and then reverses as the specular point is crossed. This results in a nonzero specular contribution to the integral. The phase variation near the shadow boundaries is rapid; hence surface contributions here are ignored in a stationary phase evaluation, but an exact evaluation includes them because the shadow boundaries are limits of integrations. Because the actual surface field distributions do not suddenly drop to zero as the shadow boundary is crossed, as assumed by the theory, the shadow boundaries contributions are spurious. Therefore, a stationary phase approximation of the physical optics integrals over closed surface tends to be more reliable than an exact evaluation.

With this in mind, this stationary phase result for a circular cylinder is,

$$\sigma = kal^2 \left| \frac{\sin(kl\sin\theta)}{kl\sin\theta} \right|^2 , \qquad (2.20)$$

where a is the radius of the cylinder, l is the length, and θ is the angle off board-side incidence. Equation (2.20) includes only the contribution from the curved side of the cylinder and not its flat ends, which may be included by using the prescription of equation (2.19). Equation (2.20) may be used to estimate the RCS of a truncated right circular cone if the radius a is replaced by the mean radius of the cone and l is replaced by the length of the slanted surface.

While the theory of physical optics offers a significant improvement over geometric optics for flat and singly curved surfaces, it suffers from other drawbacks. Although one obtains the proper result for most of the illuminated surface, the physical optics integral yields false contributions from the shadow boundaries, as noted above. Moreover, the theory shows no dependence on the polarization of the incident wave and yields different results when the receiver and the transmitter are interchanged. The effects contradict observation moves farther away from the specular direction. As illustrated in figure (2.11), the theory is quite accurate at broadside incidence (the specular case), but the agreement between the measurement and prediction becomes progressively worse as the scattering angle moves away from the direction. Keller's geometrical theory of diffraction (GTD) offers an improvement in both polarization dependence and the predicted values in the wide-angle regions.

GTD is a ray-tracing method assigns an amplitude and phase to fields diffracted at smooth shadow boundaries and at surface discontinuities. Because the latter are much more significant in backscattering computations than the former, we focused here on edge diffraction. The theory assumes that a ray striking as edge excites a cone of diffracted rays, as in figure (2.26). The half angle of this diffraction cone is equal to the angle between the incident ray and the edge. Unless the point of observation lies on the diffraction cone, no value is assigned the diffracted field.

The scattering direction in backscattering problems is the reverse of the direction of incidence, whence the diffraction cone becomes a disk, and the scattering edge element is perpendicular to the line of sight.

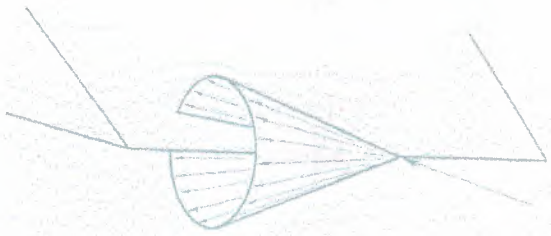

Fig.2.26. The Keller cone of diffraction rays.

The amplitude of the diffracted field is given by the product of a *diffraction coefficient* and a *divergence factor,* and the phase depends on the phase of the edge excitation and on the distance between the observation point and the diffracting edge element. Two cases are recognized, depending whether the incident field is polarized parallel or perpendicular to the edge.

The diffracted field is given by the formula,

$$E_d = \frac{\Gamma e^{iks} e^{i\pi/4}}{\sqrt{2\pi ks}\sin\beta}\left(X \mp Y\right) \ , \qquad (2.21)$$

where f is a divergence factor, X and Fare diffraction coefficients, P is the angle between the incident ray and the edge, and s is the distance to the observation point from the point of diffraction. The difference of the two diffraction coefficients is used when the incident electric field is parallel to the edge (TM polarization) and the sum when the incident magnetic field is parallel to the edge (TE polarization)

The divergence factor accounts for the decay in amplitude as the rays spread away from the edge element and includes the effects of the radius of the edge if it is curved, as at the end of a truncated cylinder, and the radius of curvature of the incident phase front.[37] The divergence factor for a two-dimensional edge (of infinite length) illuminated by a plane wave is $\Gamma = 1/s$. The diffraction coefficients are,

$$X = \frac{\sin(\pi/n)/n}{\cos(\pi/n) - \cos[(\phi_i - \phi_s)/n]} \quad , \tag{2.22}$$

$$Y = \frac{\sin(\pi/n)/n}{\cos(\pi/n) - \cos[(\phi_i - \phi_s)/n]} \quad , \tag{2.23}$$

where ϕ_i and ϕ_s are the angles of the planes of incidence and scattering, as measured from one face of the wedge, and n is the exterior wedge angle normalized with respect to π; see Fig. 2.27. The three-dimensional result for an edge of finite length f may be obtained by inserting equations (2.22) and (2.23) in equations (2.21), using equation (2.21) for V/Vo in equation (2.2), and then inserting equation (2.2) in equation (2.3).

Figures (2.28) and (2.29) compare measured and GTD predicted RCS patterns of a right circular cone frustum. The theory replicates most of the pattern features for both polarizations but fails in three different aspect angle regions. These aspects are the specular directions of the flat surfaces at either end of the frustum (0 and 180° on the charts) and near the specular flash from the slanted side at 80. The failure is due to a singularity in the diffraction coefficient Y along the reflection boundary, and a similar singularity occurs in the diffraction coefficient along the shadow boundary, a situation encountered in forward scattering.

The singularities are overcome in the *physical theory of diffraction (PTD)* by P. Ia. Ufimtsev. (Although these publications may be difficult to find, we cite them here for completeness.) Like Keller, Ufimtsev relied on t (exact) canonical solution of the two-dimensional wedge problem,

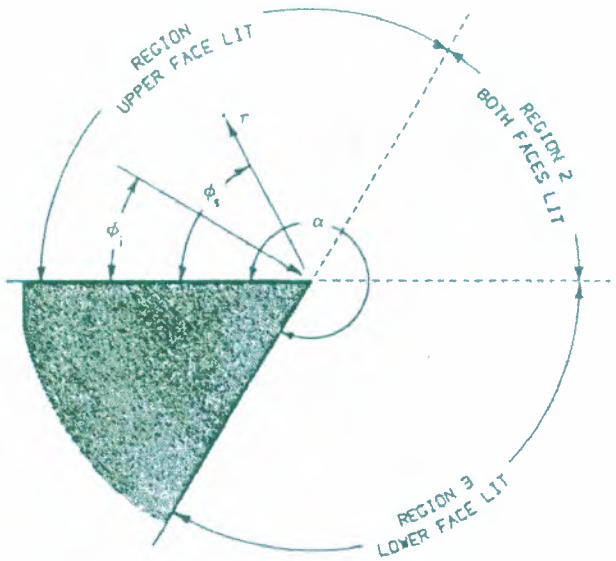

Fig.2.27. Angles of incidence and scattering for wedge geometry.

But he distinguished between "uniform" and non-uniform induced surface currents. The uniform currents are the surface currents assumed in the theory of physical optics, and the non-uniform currents are associated with the edge itself (filamentary currents). The PTD result for two-dimensional problems may be represented as a linear combination of TM and TE polarizations,

$$E_s = E_o f \frac{e^{ik\rho} e^{i\pi/4}}{\sqrt{2\pi k\rho}} \quad , \tag{2.24}$$

$$H_s = H^o g \frac{e^{ik\rho} e^{i\pi/4}}{\sqrt{2\pi k\rho}} \quad , \tag{2.25}$$

where ρ is the distance to the far-field observation point and f and g are,

$$f = \{(X-Y)-(X_1-Y_1)\} \qquad 0 \le f_i \langle a2p$$

$$f = \{(X-Y)-(X_1-Y_1)-(X_2-Y_2)\} \qquad \alpha - \pi\phi_i \le p \tag{2.26}$$

$$f = \{(X-Y)-(X_2-Y_2)\} \qquad \pi\phi_i \le a$$

$$g = \{(X+Y)-(X_1-Y_1)\} \qquad 0 \le f_i \le a2p$$

$$g = \{(X+Y)-(X_1-Y_1)-(X_2-Y_2)\} \qquad \alpha - \pi\phi_i \le p \qquad (2.27)$$

$$g = \{(X+Y)-(X_2-Y_2)\} \qquad \pi\phi_i \le a$$

The subscripted coefficients are known as the *physical optics diffraction coefficients,*

$$X_1 = -\tan[\alpha - (\phi_s + \phi_i)/2] \ , \qquad (2.28)$$

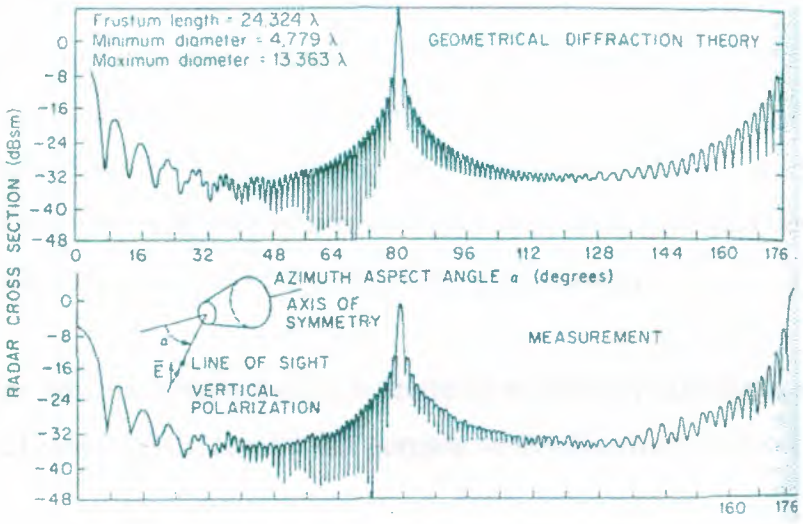

Fig.2.28 RCS of a cone frustum, vertical polarization

$$Y_1 = -\tan[(\phi_s + \phi i)/2] \ , \qquad (2.29)$$

$$X_2 = \tan[(\phi_s - \phi_i)/2] \ , \qquad (2.30)$$

$$Y_2 = -\tan[\alpha - (\phi_s + \phi_i)/2] \ , \qquad (2.31)$$

Because the PO diffraction coefficients depend on whether the upper face, the lower face, or both faces of the wedge are illuminated by the incident wave, the diffraction coefficients are combined differently in the three recognizable sectors defined in equations (2.26) and (2.27). And because surface terms have been suppressed explicitly by the subtraction of the PO coefficients, the effects of surface currents (as

distinguished from filamentary edge currents) must be accounted for independently. Those surface terms may be obtained, for example, by using geometrical optics or, paradoxically, the theory of physical optics after the edge terms themselves have been computed.

GTD and PTD are both based on the exact solution of the two-dimensional wedge problem, for which the directions of incidence and scattering are perpendicular to the edge. When extended to the case of oblique incidence, the direction of observation must lie along a generator of the Keller cone depicted in figure (2.26). If the edge is straight and of finite length, as in the three-dimensional word equation (2.3) provides an approximation of the RCS. If the edge is curved, it may be regarded as a collection of infinitesimally short segments butted together, and the scattered fields may be computed via an integration of incremental fields diffracted by each element of the edge. This is the concept introduced by Mitzner, and the summation of the fields diffracted by the edge elements implies an integral around the edge contour. (Although Mitzner's most significant results are embedded in a government document of limited distribution, we include this source in our references because of its significance.

However, Mitzner sought the fields scattered in arbitrary directions, not just those along the local Keller cones, and for this purpose he developed his concept

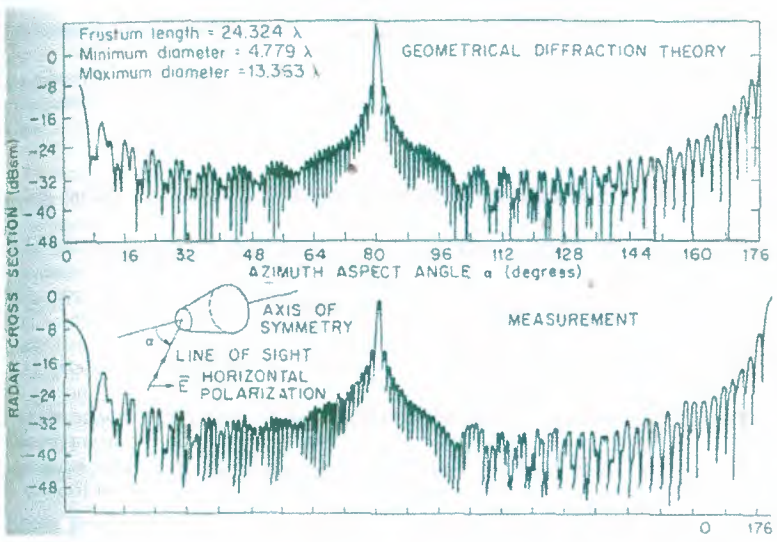

Fig.2.29. RCS of a cone frustum, horizontal polarization

Extending the example provided by Ufimtsev, he devised a set of diffraction coefficients for arbitrary directions of incidence and scattering. Not unexpectedly, those coefficients are more complicated than the X's and Y's appearing in equations (2.22) and (2.23), and (2.28) through (2.31)

Minter expressed his result as the diffracted electric-field components parallel and perpendicular to the plane of scattering in terms of the components of the incident electric field parallel and perpendicular to the plane of incidence. As such the diffraction coefficients may be expressed as three separate pairs representing parallel-parallel, perpendicular-perpendicular, and parallel-perpendicular (or perpendicular-parallel) combinations. One member of each pair is due to the other surface current on the diffracting edge (including the assumed filamentary edge currents), and the other is due to the uniform physical optics currents. Mitzner subtracted one member of each pair from the other, thereby retaining the contributions from the filamentary currents alone.

The results have identically the form of expressions, in which the PO coefficients are subtracted from the non-PO coefficients. Thus, Mitzner expression for the scattered field contains only the contributions from the filamentary edge currents. In applying his theory to scattering objects, therefore, the contributions of non-filamentary induced surface currents must be accounted for separately, just as in Ufimtsev physical theory of diffraction. When the directions of incident and scattering become perpendicular to an edge, the perpendicular-parallel terms disappear and Mitzner diffraction coefficients then reduce identically to Ufimtsev.

Undertaking what he called a more rigorous evaluation of the fields induced on a wedge, Michaeli duplicated Mitzner result for the total surface currents, confirming Mitzner prior development, but he did not explicitly remove the PO surface-current contributions. Thus, like Keller X and Y, Michaeli diffraction coefficients become singular in the transition regions of the reflection and shadow directions. Michaeli later investigated the removal of the singularities the cleverest of which was the use of a skewed coordinate system along the wedge surfaces.

While these methods of evaluating the fields scattered by edge elements may be applicable to smooth unbounded edges, they do not account for the discontinuities at

corners where the edges turn abruptly in other directions. An attack on the problem has been suggested by Sikta et al.

When applying these approximate high-frequency methods of estimating the fields scattered by complex objects, it is necessary to represent the object as a collection of surfaces having relatively simple mathematical descriptions. The actual surface profiles may be approximated by segments that have conveniently simple mathematical descriptions, such as flat plates, truncated spheroids, and truncated conic sections. The total RCS may be formed by summing the field contributions of the individual segments using the methods described above or whatever other tools are available. It is important to sum the field strengths of the individual contributions, complete with phase relationships, before squaring to obtain the total RCS as given by equation (2.1).

This is tantamount to forming the coherent sum

$$\sigma = \left| \sum \sqrt{\sigma_p} e^{i\phi_p} \right|^2 , \tag{2.32}$$

where σ_p is the RCS of the *pth* contributor and ϕ_p is its relative phase angle, accounting for the two-way propagation of energy from the radar to the scattering feature and back again. If all phase angles are equally likely, one may form instead the non-coherent sum,

$$\sigma = \sum \sigma_p , \tag{2.33}$$

The non-coherent RCS is meaningful only if a change in the aspect angle or a sweep in the instantaneous radar frequency does indeed result in a uniform distribution of phase angles. It is the average RCS formed over a time interval long enough to ensure the equal likelihood of all phase angles.

2.4 RCS Measurement Techniques

RCS measurements may be required for any of several reasons, ranging from scientific inquiry to verification of compliance with product specifications. There are no formal standards governing instrumentation and measurement methods, but informal standards of good measurement practice have been recognized for decades. Depending on the size of the test object, the frequencies to be used another test requirements, measurements may be made in indoor test facilities or on outdoor ranges. Because one is seldom interested in the RCS of an object for only one aspect angle, all static test ranges use turntables or rotators to vary the target aspect angle. Although the purpose of testing often governs how the measurements will be made.

2.4.1. General Requirements

The most important requirement for RCS measurements is that the test object be illuminated by a radar wave of acceptably uniform amplitude and phase. Good practice dictates that the amplitude of the incident wave deviates by no more than 0.5 dB over the transverse and longitudinal extent of the target and that the phase deviation be less than 22.5°. It is standard practice at some test ranges to physically probe the incident field at the onset of a test program to verify the amplitude uniformity of the incident wave.

The phase requirement is the basis of the far-field range criterion

$$R \rangle 2D^2 / \lambda \quad , \tag{2.34}$$

where R is the distance between the instrumentation radar and the test object and D is the maximum target dimension transverse to the line of sight. All other error sources being fixed, compliance with the far-field requirement is generally felt to yield data with an accuracy of 1 dB or better. Figure 2.30 illustrates the far-field requirement for a variety of frequencies and targets.

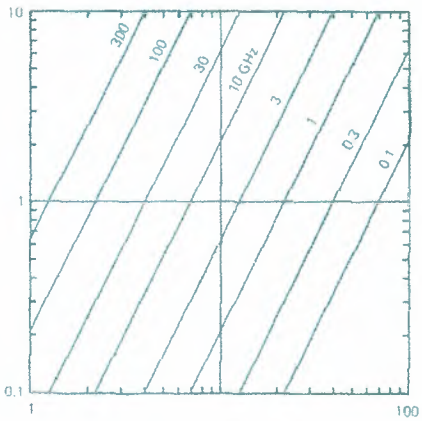

Fig.2.30. The far-field distance.

Errors attributable to radar instrumentation should be held to 0.5 dB or less, which requires careful design and selection of components. The drift in system sensitivity should exceed this value for the time it takes to record a single RCS pattern, which sometimes may approach an hour. The dynamic range of the system should be at least 40 dB, with 60 dB preference. Linearity over this range should be 0.5 dB or better, and if not steps should be taken to correct measured data via calibration of the receiver transfer function (gain characteristics).

RCS measurements should be calibrated by the *substitution method,* in which an object of known scattering characteristics is substituted for the target under test. Given the known (measured or calibrated) receiver gain characteristics, this establishes the constant by which a receiver output indication may be convened to an absolute radar cross-section value. Common calibration targets include metal spheres, right circular cylinders, flat plates, and corner reflectors. The radar cross sections of these objects may be calculated by using the expressions
given in Section (2.3).

Because residual background reflections contaminate the desired target echo signal, they should be minimized by careful range design and operation. Interior walls of indoor test chambers must be covered with high-quality radar-absorbing material, and the surface of the ground on outdoor ranges should be smooth and free of vegetation. Target support structures should be designed specifically for low echo characteristics.

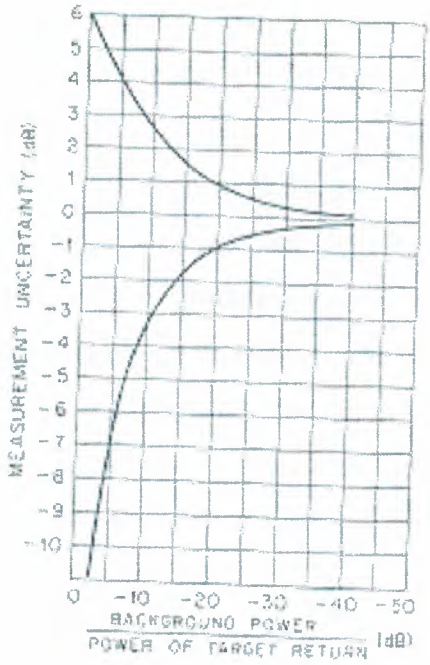

Fig.2.31. Measurement error as a function of the relative background power level.

The effects of undesired background signals are illustrated in figure (2.31). Because the relative phase between the background signal and the target signal is unknown, two curves are shown; they correspond to perfect in-phase and out-of-phase conditions. If the background signal is equal to the target signal (ratio of 0 dB) and the two are in phase, the total received power is 4 times the power due to either one. This is the value shown at the upper left of the chart (6 dB). If the two are out of phase, they cancel each other and there is no signal at all (off the lower left of the chart). The chart shows that if the error due to background signal is to be 1 dB or less, the background must be at least 20 dB below the signal one intends to measure.

Three different kinds of support structures have been demonstrated to be useful in RCS measurement. They are the low-density plastic foam column, the string suspension harness, and the slender metal pylon. The echo from a plastic foam column arises from two mechanisms. One is a coherent surface reflection, and the other is a non-coherent volume contribution from the thousands of internal cells comprising the foam material. The column should be designed so that its surfaces are never closer than 5 to 10° to the line of sight to the radar (depending on frequency), thereby minimizing the effect of the surface reflection. The non-coherent volume return is irreducible, however, and is not

influenced by the orientation of the column. The volume return of suitable foam column support materials is of the order of -58 dBsm/ft^3 of material at 10 GHz.

String suspension methods are best implemented indoors, where an overhead support point is normally available, although one documented design was seriously considered for outdoor use. One of three configurations may be selected, all requiring a custom made sling or harness to support the target. The first uses a single overhead support point and guy lines to a floor-mounted turntable to rotate the target. The second configuration suspends the target from an overhead turn table, reducing the guy lines *radiation is the most costly, using a pair of turntables slaved together, one in the ceiling* and one on the floor.

The echo signal from a string depends on the length and diameter of the string, its tilt angle with respect to the incident wave, and its dielectric constant. No matter what the tilt of the string, it will be presented normal to the line of sight twice in a complete rotation of the target and may cause spike in the RCS pattern that could be erroneously attributed to the target unless otherwise accounted for. The RCS of a string rises with fourth power of its diameter in the Religh regions (see figure 2.5), and for a given tensile strength the diameter rises only as the square root of the load to be supported. Thus, because the echo signal increases with the square of the load-caring capacity, string suspension techniques are best suited for measurements of light objects or at low frequencies.

The metal target support pylon was first suggested in 1964, but a practical implementation of the concept did not appear until 1976. The configuration of the pylon is sketched in figure (2.32), and it owes its electromagnetic performance to the sharpness of its leading edge and its tilt towards the radar (to the left in the diagram). Pylons as tall as 95 ft have been built, and it is customary to treat them with radar-

value of the target. Most of the rotators for these pylons are dual-axis, azimuth-over-elevation designs. When measurements are made with the azimuth rotation angle tilted back (away from the radar), parts of the target may sweep through the shadow cast by the top of the pylon, possibly degrading the measurements. One way to avoid this is to invert the target and tilt the rotation axis toward the radar instead of away from it. This requires the installation of the rotator in the top of the target as well as in the bottom. The unused internal cavities created for such installations must be concealed by covers or shields.

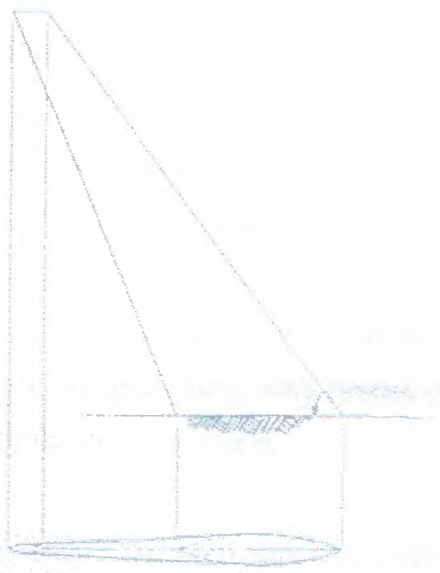

Fig.2.32. The metal support pylon. The design is for an incident wave arriving from the left.

It is often necessary to measure scale models, which requires the application of scaling laws. Because non-conducting materials must be scaled differently than good conductors, it is not possible to satisfy all the scaling requirements for arbitrary targets composed of conducting and non-conducting materials. Most targets requiring scale-model testing, however, are dominantly metallic, for which the perfectly conducting scaling law is generally regarded as adequate.

When normalized with respect to the square of the wavelength, the RCS patterns of two perfectly conducting objects of identical shape but different size will be identical if the objects are the same number of wavelengths in size. If a model is one-tenth of full

scale, for example, it should be measured at one-tenth of the full-scale wavelength (10 times the full-scale frequency). The RCS of the full-scale target may be obtained from the scale-model measurements by multiplying the scale-model RCS by the square of the ratio of the two frequencies. In this example, that factor is 10^2, or 20 dB.

2.4.1.1. Outdoor Test Ranges

Outdoor test ranges are required when test targets are too large to be measured indoors. The far-field criterion often requires that the range to the target be several thousand feet (see Figure 2.30). Because the typical target height above the ground is a few dozen feet at best, the elevation angle to the target as seen from the radar is 1° at most and often less. At such low grazing angles the ground is strongly illuminated by the antennas, and unless the ground bounce can be suppressed, the target will be illuminated by a multi-path field. In the design of an outdoor test range, therefore, a decision must be made whether to exploit the ground bounce or to attempt to defeat it. It is generally easier to exploit it than to eliminate it.

Test ranges designed to exploit the multi-path effect may be asphalted to improve the ground reflection, although many ranges are operated over natural soil. Paving the range ensures uniformity in the characteristics of the ground plane from day to day and extends its operational usefulness to higher frequencies than might otherwise be possible. A conducting screen embedded in the asphalt may improve the reflection. Paving also reduces maintenance of the ground plane, such as might be required by periodical removal of vegetation and smoothing out windblown ridges in unstable soil.

The angle of incidence and the dielectric properties of asphalt and natural soil are such that the phase of the voltage reflection coefficient is within a few degrees of 180°. This being the case: one can usually choose a combination of target and antenna heights such that the wave reflected by the ground arrives at the target in phase with the wave propagated directly from the antennas. The indirect path should be a half wavelength longer than the direct path, resulting in the following rule for selecting the antenna and target heights:

$$h_a h_t = \lambda R / 4 \quad , \tag{2.35}$$

where h_a and h_t are the antenna and targets heights, respectively, and R *is* the range to the target.

Because most test ranges have turntables or target pylons installed at a few fixed locations relative to a permanent radar complex, the range *R is* usually restricted to a few preset values. The target is installed at a height *h,* high enough to minimize spurious interactions with the ground, yet low enough to minimize the size and complexity of the target support structure. Therefore, it is the antenna height ha that is most easily controlled and adjusted to optimize the location of the first lobe in the vertical multi-path interference pattern. This is easily accomplished by mounting the radar antennas on carriages that can be raised or lowered along the side of a building or a tower provided for that purpose.

The ideal ground plane offers a theoretical sensitivity enhancement of 12 dB over identical measurements made in free space. The actual enhancement is usually significantly less than this, however, primarily because of the directivity of the antennas and imperfections in the ground plane. The directivity of the antennas precludes the target ever being squarely along the bore-sight of both the real antenna and its image in the ground plane at the same time, and the reflection coefficient of typical ground planes varies from 95 percent to as low as 50 percent or less. For all except very high and very low frequencies (millimeter wavelengths and VHP), typical sensitivities are of the order of 7 to 10 dB above free space instead of the ideal 12 dB.

When the range to the target is relatively short and tests must be performed over a wide range of frequencies, it is sometimes advantageous to attempt to defeat the ground-plane effect. One option is to install a beam shaped like an inverted V running between the radar and the target. The purpose of the slanted top of the beam is to deflect the ground-reflected wave out of the target zone. Another option is to install a series of low *radar fences* across the range. The design objective is to block ground-reflected rays from reaching the target from the radar, and vice versa, by shielding the specular

zone on the ground from both. The near sides of the fences should be slanted to deflect energy upward, and may be covered with absorbing material. It is difficult, however, to prevent diffraction of radar energy from the top of the fences from reaching the target zone or to prevent target-diffracted signals from reaching the radar receiver via the same kind of mechanism.

Because of the large distances from the radar to the target on outdoor ranges, instrumentation radars typically develop peak signal powers ranging from 1 to 100 kW. Most of them emit simple pulsed waveforms whose pulses are from 0.1 to 0.5 p s wide, with pulse repetition rates of a few kilohertz. The radiated pulse should be wide enough to completely bracket the target but short enough to minimize background clutter contributions. To reduce measurement, time and target exposure to weather or unauthorized observation, several instrumentation radars may be operated tenuously. The radars may be triggered simultaneously or may be operated simultaneously depending on the particular requirements imposed at a given installation. Stepped –or swept frequency wave form may be employed to collect coherent test data for diagnostic purpose, as discussed in the next subsection.

2.4.1.1.1. Test Ranges

Indoor test ranges offer protection from weather and therefore more productive testing, but unless a very large facility is available, maximum target sizes are limited to a dozen feet or so, because of the proximity of the walls, floor, and ceiling, they must be covered with high-quality absorbing material. The lower the intended frequency of operation, the more expensive the absorber becomes. Absorber reflectivity ratings of -50 dB are common among the materials used. This performance is usually achievable only with the pyramidal design.

Early indoor chambers were rectangular in shape, and despite the installation of good absorbent materials on the walls, RCS measurements could be contaminated by wall reflections. The most sensitive part of the anechoic chamber is the rear wall, which

receives 95 to 99 percent of the power radiated by the radar; hence one's best absorber should be reserved for the rear wall.

The floor, ceiling, and sidewalls also contribute errors, via a quadruplet of reflections not unlike those due to the ground plane of outdoor ranges. A remedy is the tapered anechoic chamber, which eliminates most of the sidewall reflections purely by means of geometrical control.

Even targets of modest size cannot be measured at the far-field distance in indoor facilities because most chambers are not much more than 100 ft or so in length. It is possible, however, to provide the necessary uniformity of illumination by *collimating* the radiated beam. This can be done by inserting a lens between the radar and the target or by reflecting the radar beam off a collimating reflector. The concept is known as the *compact range* because a beam of parallel rays can be generated in a much shorter distance than would be possible without the collimating device.

Two successful lens designs have been documented. The surface profiles of both were truncated hyperboloids of revolution, as suggested in figure (2.33), with the vertex facing the radar. While successful for the particular application they were designed for, these two lenses were too small (1.1 and 0.43 m in diameter) for most targets of interest.

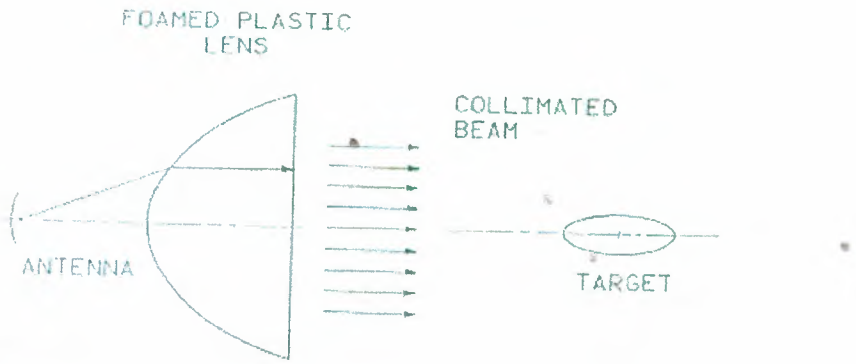

Fig.2.33. A compact range uses a microwave lens to collimate a beam into parallel rays. The lens surface is hyperboloid of revolution.

Because the flat rear face of the lens is parallel with the phase fronts there, it can be a significant source of undesired reflections. The rear-face reflections may be

reduced by tilting the lens slightly, at the price of slight aberrations in the phase of the incident field. (Lenses also can be made with both surfaces curved, as is routinely done in the visible portion of the spectrum.) Lenses may be made of foamed plastic, and the dielectric constant of the material and the desired focal length determine the profile the lens must have. The uniformity required of material properties throughout the volume of lens, whether made of foamed or of solid plastic, has thus far discouraged the fabrication of larger versions.

The reflector offers a different way to collimate a beam. In contrast to the lens, which is placed between the radar and the test object, the radar and the test object remain on the same side of the reflector, as shown in Fig. (2.34).The reflector is typically an offset parabolic, meaning that the parabolic surface does not include the vertex of the generating parabola. This permits the feed that excites the reflector to be placed out of the beam reflected toward the target. If the test object is held within one or two focal lengths of the reflector and if the reflector is excited by a suitably designed feed, the reflected wave is sensibly planar.

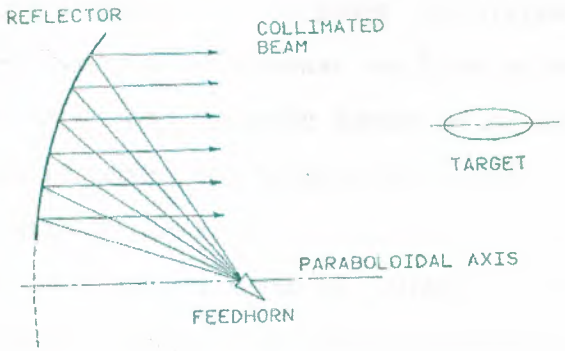

Fig.2.34. A compact range using an offset parabolic reflection

However, unless the edges of the reflector are carefully designed, the incident field in the target zone will be contaminated by fields diffracted from the edges of the reflector. The diffraction causes ripples in both the amplitude and the phase of the field distribution in the target zone. In some cases the effect is small enough to be ignored, but in high-quality installations the ripple may be objectionably large. Rolled-edge configurations that appear to have acceptable performance have been designed and tested. The price paid for this improvement in performance is a much larger and more complicated reflector structure.

Targets measured indoors are placed much closer to the radar than those measured outdoors, and useful measurements may be made by using much less radiated power. Early indoor instrumentation radars relied on simple CW sources, and undesired chamber reflections were suppressed by a cancellation process. The procedure is to prepare the chamber for a measurement in every respect except for the installation of the target on its support fixture. A small sample of the transmitted signal is passed through a variable attenuator and a variable phase shifter and combined with the received signal. The amplitude and phase of the signal sample are then adjusted so as to cancel the signal received in the absence of the target.

The availability of low-cost, phase-locked, frequency-synthesized sources now makes it attractive to collect wideband RCS data, which contains far more target-scattering information than CW measurements made at single frequencies. When coherent RCS scattering data is suitably processed, it is possible to generate *radar imagery*, two-dimensional maps of the echo sources of test objects.

Figure (2.35) is an example of such an image. The processing required to generate this image is a double Fourier transformation, one from the frequency domain to the time domain and the other from the angle domain to the cross-range domain. The frequency-time domain processing may be performed virtually in real time (a second or two for processing and display on a video screen), but the conversion from the angle domain to the cross-range domain must be performed offline. The fast Fourier transform (FFT) is invariably exploited to expedite the processing.

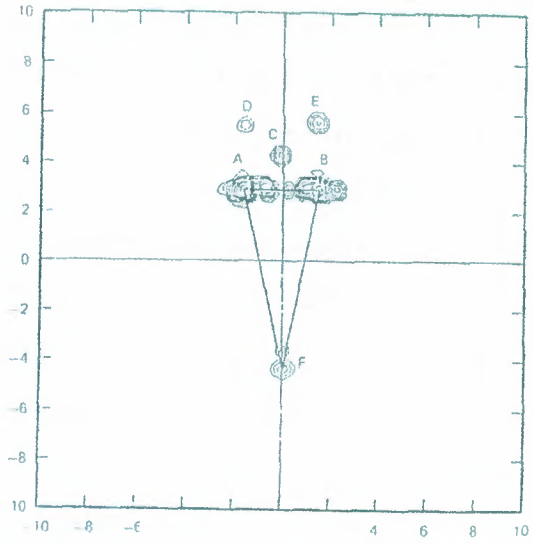

Fig.2.35. Radar image of a wedge

The resolution of the processed image in the time (range) domain is inversely proportional to the bandwidth of the emitted waveform. The resolution in the cross-range domain is inversely proportional to the aspect angle window over which the data is collected. Thus, the operating characteristics of the instrumentation system and the azimuthally data sampling rate must be decided before the data is collected. Because the cross-range coordinate of the resulting image is perpendicular to the axis of rotation of the target, it may be necessary to multiply that coordinate by a scale factor that effectively registers the generated image with, say, a plan view of the target.

The resulting data may be presented in the form of a contour map, as in figure (2.35), or in a gray-scale pixel format. The wedge target has been superposed in the figure for diagnostic purposes, and the particular attitude shown is for edge on incidence. Images like this can be generated for any angle of incidence, provided the target has been rotated through a sector wide enough to yield the desired cross-range resolution and has been sampled at a sufficient number of angles over that sector, say, 64, 128, or 256 samples. In practice, the target is rotated continuously while the swept- or stepped frequency data is collected. The angular speed must be slow enough that the phase of the return at the end of a frequency sweep due to target motion be within 22.5° from what it would have been had the target not moved.

Note that the leading edge of the wedge is an identifiable scatterer, although much less intense than the contributions from the base. In addition to the direct echoes *A* and *B* due to single diffraction from the base, there are additional contributions due to cross-base (multiple) diffraction. Contribution C is due to the excitation of one edge of the base by the other, which then diffracts the energy back to the source. This involves a single traverse across the base, and the phase delay due to the additional path length places the apparent source of scattering behind the actual base by half the width of the base. Contribution *C* appears along the centerline because the total propagation path from the source to the first edge, then to the second edge, and then back to the source is independent of the target rotation angle.

This is not the case for contributions *D* and *E*, which are due to double traverses of the base. That is, diffraction from one edge reaches the other edge across the base, which then diffracts some of the energy back toward the first edge in a second traverse. Because the diffraction responsible for contributions *D* and *E* crosses the base twice, *D* and *E* appear precisely one base width behind the actual base. Unlike contribution *C*, which lies along the centerline, *D* and *E* are displaced to the side, appearing directly behind the base edges. This is so because the phase of the excitation of the primary edge varies as the edge is moved toward or away from the source by the target rotation.

These "ghost" scatterer owe their existence to the way in which the data-processing system sorts the range and cross-range locations of scatterers. Down-range locations are sorted according to their processed time delays and cross-range locations according to their time-delay rates, whether due to real scatterers or to interactions between scatterers. Even though the contributions of some scattering centers may involve propagation in directions other than along the line of sight from the radar, the system has no way of discerning the fact. Therefore, despite the powerful diagnostic value of images like these, one must always be aware that multiple interactions between target elements can create scattering sources that are not where they appear to be.

CHAPTER 3

RADAR CROSS SECTION ENHANCEMENT

3.1. Introduction

Some practical applications require enhancement of the RCS. For example, when an aircraft or satellite is tracked, we want a constant return during the tracking period, thereby necessitating augmentation of the RCS of the vehicle in some reselected range of angles. Passive RCS augmentation devices are used to enhance the returns from small vehicles and deception devices; for example, light aircraft, buoys, small boats, or missile targets. For scattering and remote-sensing measurements RCS augmentation is used for calibration targets like corner reflectors.

An RCS augmenter is an integrated device with or without a lens and a retro-reflecting surface; and it can be a mono static or a bistatic device. In general, there are three methods for achieving RCS enhancement. First is the proper shaping of the target to present a large echo area over the ranges of parameters of interest; this method is least useful for airborne targets. The second is the use of impedance loading at selected points on the target to disturb the induced current so as to achieve the goal; this method generally is limited to the narrow band. The third is the addition of a Pre-designed RCS augmentation device to the target to meet the specific requirements.

In this chapter we present different methods of RCS enhancement and describe different practical devices for RCS augmentation, including their key design considerations. Important characteristics of some standard devices also are presented.

3.2 Corner Reflector

Corner reflectors are structures formed with two or three metal plates. Figures 3.1(a), (b) shows some dihedral and trihedral corner reflectors, respectively. Though these devices are passive, due to multiple scattering effects they have considerably large mono static and bistatic RCS over a relatively wide range of aspect angles; one typical multiple scattering path ABCD is shown in figure 3.1(a). A dihedral corner reflector

gives large RCS only in the plane perpendicular to the reflector; for example, in the x y-plane in figure 3.1(a). This can be improved, and the structure can be made 10 provide large RCS in other planes by addition of a third plate, as shown in figure.1(b). Depending on the shape of the plates, the trihedral corner reflectors are cal
square trihedral, triangular trihedral, or circular trihedral corner reflectors.

3.2.1. Dihedral Corner Reflectors

Recently, several authors reported extensive work performed on dihedral corner reflectors. Corona et al. [discussed a mathematical model using the physical optics considerations and the effects of illumination of one face by the rays diffracted by the edge of the other face. Table (3.1) lists the key RCS formulas and angular coverage for dihedral corner reflectors.

The physical optics backscattered field due to the dihedral corner reflector, shown in figure (3.1-a), illuminated by a plane wave with perpendicular polarization (i.e., E-field in the z-direction, xy-plane being the plane of incidence) is given by

$$E_{\perp}^{PO} = -\frac{ik}{4\pi}\frac{e^{-ikr}}{r}2abE_{\perp}^{i}\left[\Gamma_{\perp}^{x}\sin\varphi\frac{\sin(ka\cos\varphi)}{ka\cos\varphi}e^{ika\cos\varphi}+\Gamma_{\perp}^{y}\cos\varphi\frac{\sin(ka\sin\varphi)}{ka\sin\varphi}e^{ika\sin\varphi}+2\Gamma_{\perp}^{x}\Gamma_{\perp}^{y}\sin\varphi\right] \tag{3.1}$$

Particulars	Radar Cross Section
Dihedral reflector Monostatic Broadside incidence	$\sigma \approx \frac{4\pi A_e^2}{\lambda_0^2}$ (A_e = area of projected aperture on the incident ray)
Dihedral reflector Monostatic Angular coverage ± 30°	$\sigma = \frac{4\pi a^2 b^2 \sin^2(\pi/4+\phi)}{\lambda_0^2}$ (see Figure 3.1(a)) First-order PO formula. Polarization effects not accounted for.
Dihedral reflector Bistatic	$\sigma(\beta) = \sigma(0)\,e^{-2\nu\beta}$ β = bistatic angle ν = design parameter given by Peter's design curve [1]

where $E_i^{\perp}$ is the amplitude of the incident electric field,

$$\Gamma_{\perp}^{x} = \frac{Z\sin\varphi - 1}{Z\sin\varphi + 1}\ , \tag{3.2}$$

$$\Gamma_{\perp}^{y} = \frac{Z\cos\varphi - 1}{Z\cos\varphi + 1}\ , \tag{3.3}$$

Z is the surface impedance of the reflector surface normalized to the intrinsic impedance of free space, superscripts x and y refer to the plates y = 0 and x = 0, respectively. The PO field for parallel polarization (i.e., E-field in the xy-plane) is obtained from (3.1) by replacing $E^{i}{}_{\perp}, \Gamma^{x}{}_{\perp}$ and $\Gamma^{y}\perp$ with $E^{i}{}_{II}, \Gamma^{x}{}_{II}, \Gamma^{i}{}_{II}$ respectively; and the two reflection coefficients are given by

$$\Gamma_{\Pi}^{x} = \frac{\sin\varphi - Z}{\sin\varphi + Z}\ , \tag{3.4}$$

$$\Gamma_{\Pi}^{y} = \frac{\cos\varphi - Z}{\cos\varphi + Z}\ , \tag{3.5}$$

The scattered field expressions just given do not consider the effects of diffraction.

Detailed considerations of the diffraction effects are given in. We can show that for parallel polarization the total scattered field is given by

$$E_{\Pi} = E_{\Pi}^{PO} + \frac{ik}{4\pi}\frac{e^{-ikr}}{r}2abE_{\Pi}^{i}$$

$$\times\left\{\begin{array}{l}\dfrac{\cos\varphi - Z}{2a}e^{ika\cos\varphi}e^{-i\pi/4}\displaystyle\int_0^a \frac{1}{\sqrt{2\pi kd_1}}e^{ikd_1}e^{iky\sin\varphi} \\ \times D_h(\beta_1,\gamma_1)\left[\dfrac{T_{\Pi}(\alpha_1)}{Z}\right]dy + \dfrac{\sin\varphi - Z}{2a}e^{ika\sin\varphi}e^{-i\pi/4} \\ \times\displaystyle\int_0^a \frac{e^{-ikd_2}}{\sqrt{2\pi kd_2}}e^{ikx\cos\varphi}D_h(\beta_2,\gamma_2)\left[\frac{T_{\Pi}(\alpha_1)}{z}\right]dx\end{array}\right\}, \tag{3.6}$$

$$T_{\Pi}(\alpha) = \frac{2Z\cos\alpha}{Z + \cos\alpha}\ , \tag{3.7}$$

and $D_h(\beta,\gamma_1), D_h(\beta_2,\gamma_2)$ are hard diffraction coefficients for parallel polarization; the diffraction process involved for this case is shown in Figure 3.2(a), which represent the top or bottom view of the dihedral reflector shown in figure.

Figure 3.1(a) and (b) show the backscattered field patterns for perpendicular parallel polarizations, respectively, for a perfectly conducting corner reflector With a/X = 5. The fields shown are normalized with respect to the GO maximum value.

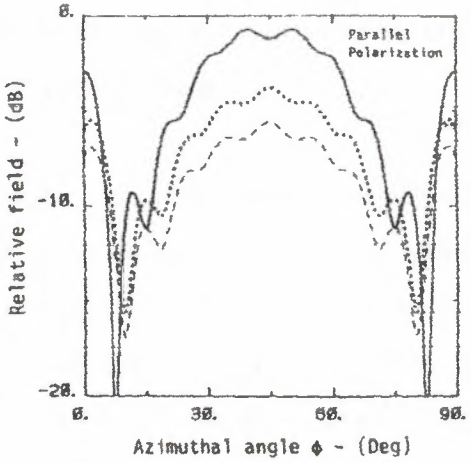

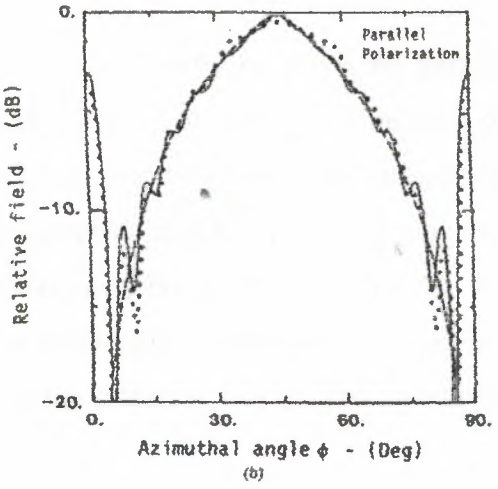

Fig.3.1. Back-scatted field (dB normalized to GO maximum value) versus the azimuthal angle ϕ by a perfectly conducting 90 dihedral corner with a/λ : (a)perpendicular parallel ; (b) parallel polarization.

Physical optics analyses of dihedral corner reflectors are given in; PTD analysis is discussed in; and the effect of higher order reflections and diffraction also are described in; Details of these considerations will not be discussed here. We shall present only a few important experimental results and their relationship with appropriate theoretical results. Figure (3.2) gives the experimental and theoretical RCS normalized to 1 m patterns for a 90° dihedral corner obtained under a variety of conditions. Researchers have found that a 90° dihedral corner has Wide beam width of RCS pattern if ripples in excess of 5 dB only are of concern, particularly for horizontal polarization. When the reflector angle is not 90°, the pattern splits into several beams giving rise to large variations in the RCS with aspect angle.

Effects of the bistatic angle on the relative echo signal from a normal corner reflector and a corner reflector with 5°-error are shown in figure 3.3(a) and (b), respectively. The results indicate that for larger bistatic angles the reflector error generally increases the beam width of response. Normally, for the bistatic case, a large beam width is difficult to achieve without reduction of the cross section. However, the results of figure (3.3) tend to indicate that it may be possible to obtain fairly large mono-static and bistatic RCS by using a cluster of reflectors because here the degradation of the reradiated pattern will be confined to one plane.

To understand this, we must briefly examine the polarization characteristics of dihedral corner reflectors. A linearly polarized wave incident on the reflector, with the electric vector either parallel or perpendicular to the seam of the reflector, is reflected with the same polarization, provided that the wave suffers an even number of bounces at the reflector. Similarly, a circularly polarized incident wave will also be reflected with the same sense of circular polarization. Polarization sensitivity of the dihedral corner reflector can be utilized for the calibration of the cross-polarization receiver of a linear dual-polarized radar.

3.2.2 Trihedral Corner Reflectors and Wide-banding

As indicated earlier, in a plane perpendicular to the plates the dihedral corner reflector provides maximum RCS over- a range of aspect angles. In other planes (i.e., for $\theta \neq \pi/2$) the performance deteriorates. Use of a third plate is necessary to maintain

nominal RCS for wide range of the aspect angle φ for variable θ. This is how the trihedral reflectors were developed. To the best of our knowledge, no accurate analysis for the RCS of a trihedral reflector is currently available. However, some experiment results and approximate expressions are available as guides for designing such reflectors.

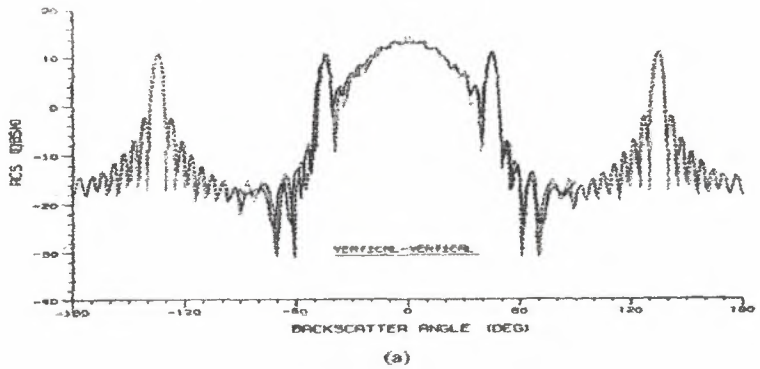

(a)

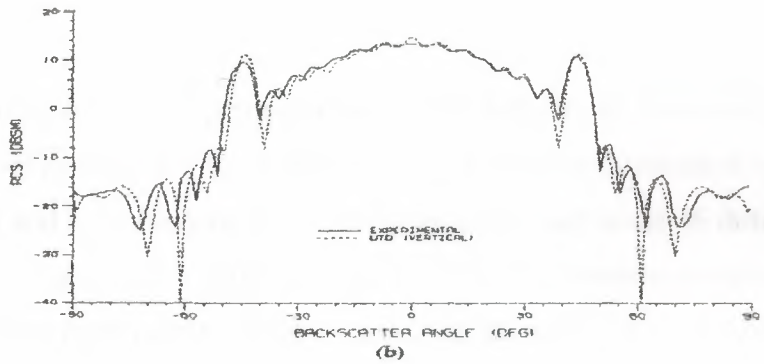

(b)

These are given in Table 3.2. Figure (3.4) shows the experimental back-scattering cross-section pattern of a triangular trihedral corner reflector for different values of 0. In Figure (3.4.3) is the bistatic angle, therefore $\beta = 0$ means the case of a scattering; the angle a, interpreted as the angle of incidence, is given by $\alpha = (\varphi - 45^{\circ})\sin\theta$ where θ and are as shown in figure (3.1) figure (3.4) indicates that peaks on the two sides of the broad pattern are attributed to the scattering effects of the corners, to reduce these effects, a compensated triangular trihedral corner reflector has been found useful; one is sketched in figure (3.6). Monostatic RCS patterns for compensated and uncompensated reflectors are shown in figure (3.7), which clearly show the effects 0 compensation. Analyses of such compensated structures are not yet available. Recently some theoretical results have appeared for the trihedral corner reflector

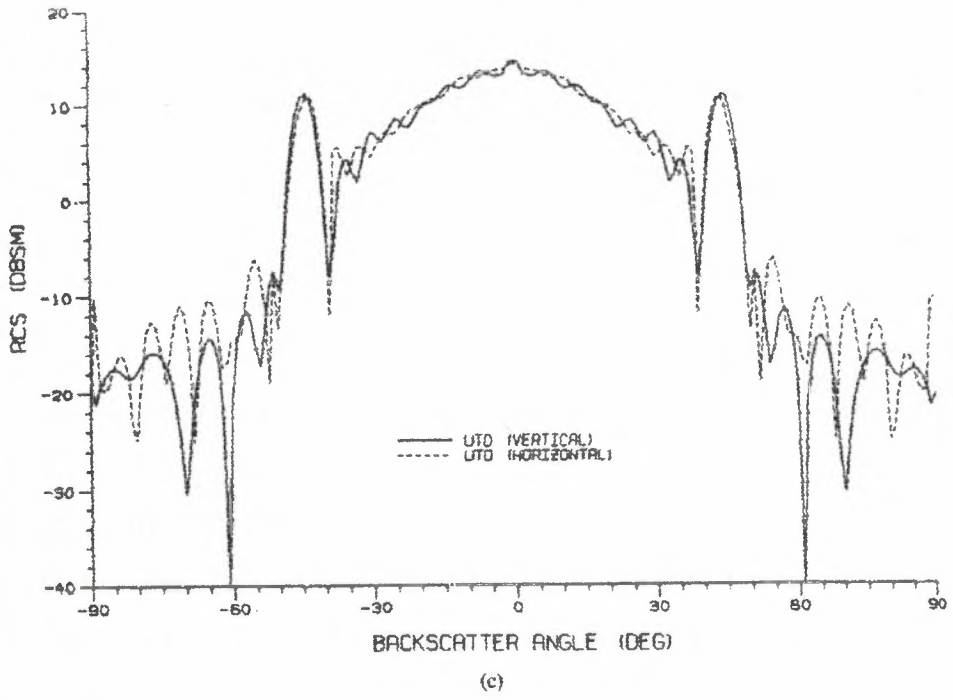

Fig.3.2. (a) Theoretical and experimental azimuthal patterns for scattering RCS of a 90 dihedral corner reflector a = b = 5.6088 λ ; f = 9.4 GHz; Polarization is vertical; (b) Experimental and UTD RCS using higher-order diffraction of the 90 dihedral corner reflector in (a), where a = b = 5.6088 λ ; f = 9.4 GHz; Polarization is vertical. (c) UTD cross section using higher-order rays for vertical polarization for the 90 dihedral, where a = b = 5.6088 λ ; f = 9.6 GHz; R=200 λ .

Figure (3.6-a) shows the trihedral corner geometry, and a comparison between the backscattered cross-section values obtained by using finite-difference time domain; an the shorting and bouncing ray codes are shown in Figure (3.7-b).

Trihedral Corner Reflector Type	Maximum RCS	Average RCS	Angular Coverage	RCS as a Function of θ, ϕ
Square	$\sigma = 12\pi a^4/\lambda_0^2$	$\langle\sigma\rangle = \frac{0.7a^4}{\lambda_0^2}$	25° cone about symmetry axis	(a)
Triangular	$\sigma = \frac{4\pi a^4}{\lambda_0^2}$	$\langle\sigma\rangle = \frac{0.17a^4}{\lambda_0^2}$	40° cone about symmetry axis	(b)
Circular	$\sigma = \frac{15.6a^4}{\lambda_0^2}$	$\langle\sigma\rangle = \frac{0.47a^4}{\lambda_0^2}$	32° cone about symmetry axis	—

3.3 DIELECTRIC LENSES

By Utilizing the properties of dielectric lenses it is possible to enhance the mono-static and bistatic RCS over a wide range of frequencies and aspect angles. Different types of lenses_ for example, Kay's spherical lenses the Eaton-Lippman lens, and more popularly the Luneberg lens—have been used for such Purposes; compared to metal targets of similar size, they provide larger mono-static and bistatic RCS. The cylindrical Eaton-Lippman lens has a normal incidence mono-static RCS equal to,

$$\sigma \approx 16\pi a^2 \left(\frac{1}{\lambda}\right)^2 , \tag{3.8}$$

where a and 1 are the radius and length of the lens, respectively. A cylindrical lens has the advantage of azimuthal symmetry without requiring a metal reflector. The limitations of such lenses are their poor elevation plane performance and their requirement for an infinite or very high-dielectric constant at the center. The latter requirement is very difficult to satisfy in practice.

3.3.1. Luneberg Lenses

An ideal structure for antenna scanning applications and RCS augmentation is symmetric configuration like a sphere; and the more popular Luneberg lens has this structure,

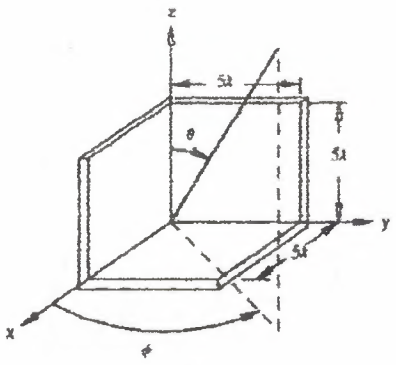

(a)

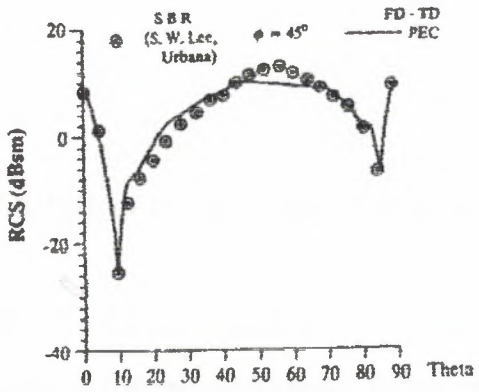

(b)

Fig.3.4. A trihedral reflector and (b) its RCS with respect angle θ, where $\phi = 45$.

A Luneberg lens, shown in figure (3.5), is a spherically symmetric inhomogeneous structure with the property that parallel rays incident on it are focused at a diametrically opposite point on its surface, and a point source located on its surface gives rise to parallel rays going out from its surface on the other side figure (3.5). The required dielectric constant of the lens varies according to radius from 2 at the center to unity at the surface. Typical ray paths in the lens are shown in figure (3.5). The refractive index n(r) at any point, r distance from the center, is given by

$$n^2(r) = 2 - \left(r/a\right)^2 \quad , \tag{3.9}$$

A practical Luneberg lens consists of several concentric spherical layers, of dielectric materials with decreasing dielectric constants.

$$\sigma_{max} = \frac{4\pi^3 a^4}{\lambda_o^4} \quad , \tag{3.10}$$

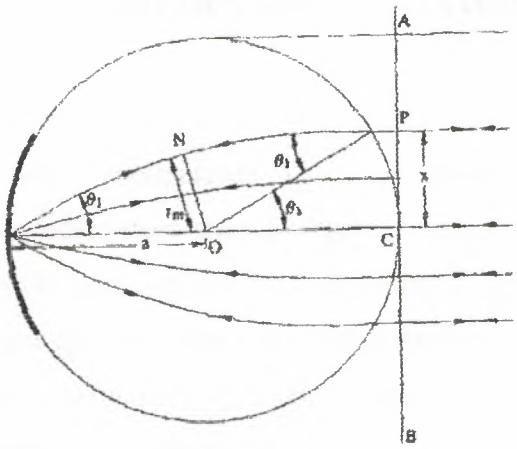

Fig.3.5. Path of the ray inside a Luneberg lens.

As an example, with a = 12.7 cm, equation (3.10) indicates σ_{max} max 31.76 m at λ_0 = 3.19 cm (9.4 Hz), whereas the measured value for σ_{max} max 31.7 m. Figure (3.6) shows the measured backscattering cross sections versus aspect angle for a number of commercially available Luneberg lenses at 9.375 GHz.

3.3.2 Luneberg Lens with a Reflector

Parallel rays incident on the Luneberg lens with a reflector, shown in figure (3.11), generally are reflected back toward the transmitter. This then augments the backscattered RCS. The reflector may be connected separately or metallized on the lens surface. The RCS may be enhanced over a large range of aspect angles by varying the size of the reflector used. Table (3.3) gives some pertinent information about different lens models along with their backscattering cross sections.

CHAPTER 4

REDUCTION OF RADAR CORSS SECTION

4.1. Introduction

An important problem often encountered in many military and civilian applications is how to reduce the radar return from a target to a specified minimum. In certain military applications, for obvious reasons, it is necessary to reduce the RCS of targets like aircraft, missiles, and spy satellites. In civilian applications, satisfactory performance of air traffic control radar requires that the scattering or reflections off the terminal buildings and aircraft hangars be reduced so that they cause less interference to the airport radars, RCS reduction finds important application also in the indoor measurements of antenna patterns and target scattering, where the required free space environment generally is simulated by reducing undesirable reflections from the surroundings.

Generally, there are four means of reducing (or controlling) the RCS of targets: target shaping, discrete loading, distributed loading, and active loading. In target shaping the shape of the target is modified to redirect the scattered energy from one angular region of interest in space to another region of little or no interest for airborne targets, any shaping subject to aerodynamic considerations may be required to satisfy stringent requirements; however, static targets are more flexible to shaping.

In discrete loading the target is loaded at selected points with passive impedances to reduce the overall cross section. The method relies on phase cancellations in certain directions and, hence, it is severely limited in bandwidth.

In distributed loading the target is coated with lossy material, known as the radar absorbing material (RAM). The lossy material absorbs, in the form of heat, a Considerable amount of incident energy and thereby reduces the RCS. For narrow bandwidths, a single coating of RAM may suffice, but broad bandwidth generally required multiple coating.

The active loading is similar to the discrete loading mentioned earlier, but uses active elements to achieve the necessary phase cancellation.

None of these techniques alone will reduce the RCS of a target below a certain minimum value under all circumstances; for example for a wide range of aspect angles, a wide band of frequencies, and both orthogonal polarizations. In most cases a judicious combination of two or more methods may be required to achieve the goal. For example a ship or a vehicle may need the shaping criterion during the engineering design followed by a properly planned local application of RAM around the possible scattering centers like the edges and other discontinuities; generally, to coat the vehicle completely with RAM is not necessary.

Different methods of reducing the RCS are discussed in this chapter. Theoretical results supported by available experimental results are discussed to illustrate the status and promise of various RCS reduction techniques. Although detailed theoretical analysis is not given, appropriate references are cited wherever possible. A few practical designs with numerical examples also are described.

4.2. Target Shaping

RCS of a target can be reduced by shaping it so that it does not project a large effective area to the radar. For flying objects, aerodynamic considerations severely restrict the choice of shapes for reduced RCS. Even for other objects, it seems impossible to shape a target so that it has a given minimum RCS for all radar parameters; for example, for all aspect angles. However, we can make some general comments. For moving objects like a ship or other vehicle, the RCS can be reduced considerably by shaping the vehicle to avoid dihedral angle corners with interior angles of 900 and so that the edges are smoothed. A mast can be designed with a polygonal cross section, which would give it an RCS lower than one with a circular cross section. When using foam columns for support, a square cross section can be used for low RCS. Generally, RCS reduction by shaping the target would assume some significance in situations where orienting the target to reduce the probability of its detection by radar is possible.

To help understand the effect of such shaping, we will briefly discuss the effect of body shape on RCS. The aim here is to help the design of an object having a maximum volume hut low (or minimum) RCS. Figure (4.1) shows the nose-on backscattering cross sections for a class of metallic objects having identical projected areas in all directions, length-to-diameter ratios, and volumes within a factor of two. The results shown in figure (4.1) indicate that RCS of bodies can vary significantly depending on their shapes.

The effect of shaping the nose of a body is of considerable practical importance. A reduction in nose-on RCS may be achieved in general by using an ogival section instead of a spheroidal section for the nose of a body. An ogive-shaped nose cone can provide considerably lower RCS than a spheroidal one.

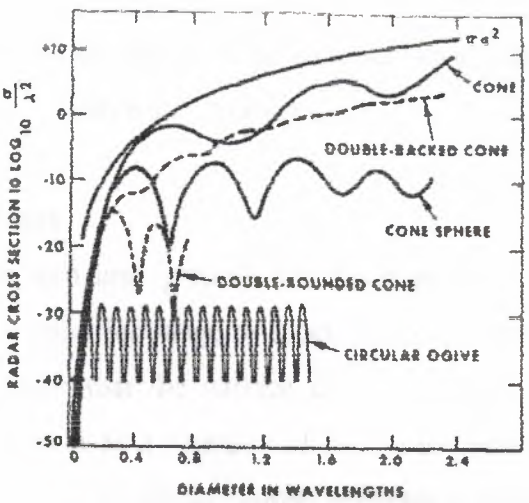

Fig.4.1. Nose-on backscattering cross section of a class objects

In aircraft, the use of shaping to achieve a low RCS usually involves a trade-off with aerodynamic performance. Note that fins and wings produce large radar returns only at normal and near-normal incidence, particularly at high frequencies. Figure (4.6) indicates that a flat plate has a large RCS under a variety of incident conditions. Curving the edges may cause less peak returns but the incident energy will be spread over a larger range of aspect angles. A second modification, uses a tapered dielectric material for a portion of the plate. A possible construction scheme for the reduction of RCS of a

rotor blade is contributions by various components to the RCS for both polarizations. At selected aspect angles, the curved fins produce less RCS than the straight fins. The "good" fin design is considered superior from the point of view of the "art" of smoothing radar returns.

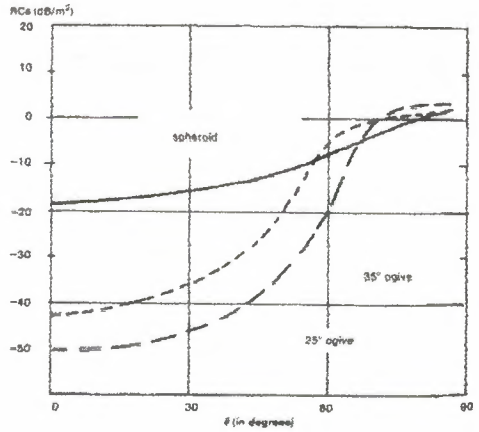

Fig.4.2. Possible modifications in the design of the nose section of the body (with RCS value at 3.0 GHz).

4.2.1. Shaping Dihedral Corners

Conducting surfaces on ship and ground vehicles may form corner reflectors having increased RCS in some specified range of aspect angles. Their radar returns can be minimized by taking due care that the surface do not meet at right angles. The required angle between the faces is as a function of RCS reduction and the electrical size of the corner. The geometry of the dihedral corner reflector is shown in figure (4.3). We assume that the dimension in a direction perpendicular to the plane of the figure (1). The basic formula used for this purpose is the bistatic scattered field for a flat rectangular metal plate of length c and illuminated by plane wave, where we assume the plate width is d (measured in a direction perpendicular to the incident plane). With the geometry given, we can show that the bistatic scattering function,

$$S = \frac{ikdc}{2\pi}\left(\hat{s}\times\hat{h}_r\right)\left(\hat{n}\times\hat{h}_i\right)e^{ikr_o(\hat{i}-\hat{s})}.\sin\frac{\left[kc\left(\sin\theta_i-\sin\theta_s\right)/2\right]}{kc\left(\sin\theta_i-\sin\theta_s\right)/2}, \qquad (4.1)$$

where

$\hat{h}_i$, $\hat{h}_r$ = the unit vectors in the directions of the incident and reflected magnetic fields, respectively,

r_o = the position vector of the midpoint of the plate with respect to the origin,

$\hat{i}$, $\hat{s}$ = the unit vectors in the direction of incidence and scattering, respectively.

The RCS of the dihedral corner figure (4.11) can be obtained from as,

$$\sigma = \frac{\lambda^2}{\pi}\left|S_a + S_b + S_{ab} + S_{ba}\right|^2 , \tag{4.2}$$

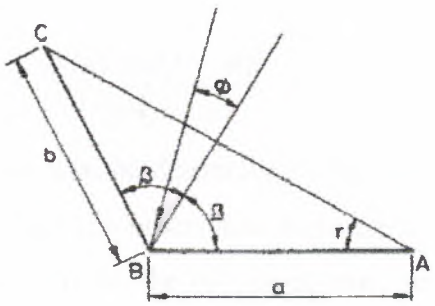

Fig.4.3. The dihedral corner reflector

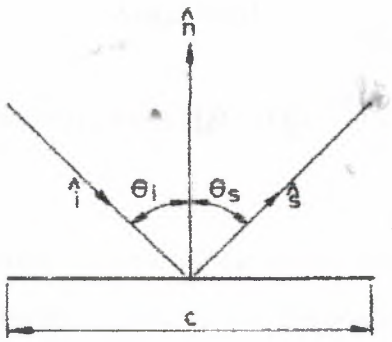

Fig.4.4. Incident and scattering directions of flat plate

where S_a and S_b are direct contributions from the faces having dimensions a and b are the double bounce contributions. With the apex of the dihedral corner placed at the origin (4. I) can be used to determine the direct contributions for
$-\beta \le \phi \le \beta$. They are

$$S_a = i\frac{ikda}{\lambda}\sin(\beta+\varphi)\exp[-ika\cos(\beta+\varphi)] \times \frac{\sin[ka\cos(\beta+\varphi)]}{ka\cos(\beta+\varphi)}, \quad (4.3)$$

$$S_b = i\frac{kbd}{\lambda}\sin(\beta-\varphi)\exp[-ikb\cos(\beta-\varphi)] \times \frac{\sin[kb\cos(\beta-\varphi)]}{kb\cos(\beta-\varphi)}, \quad (4.4)$$

The secondary contributions can be determined after finding the illumination of one face due to the reflection from the other face. Because this illumination changes with φ and β, the illuminated sectors on the two faces must be determined for each φ and β. For E-polarization, the scattering functions for double bounce are given by,

$$S_{ab} = \frac{ikb'd}{\lambda}\sin(3\beta+\varphi)\exp[-ikb'\cos 2\beta\cos(\beta+\varphi)]\frac{\sin[kb'\cos 2\beta\cos(\beta+\varphi)]}{kn'\cos 2\beta\cos(\beta+\varphi)}, \quad (4.5)$$

$$S_{ba} = -\frac{ika'd}{\lambda}\sin(3\beta-\varphi)\exp[-ika'\cos 2\beta\cos 2(\beta-\varphi)]\times\frac{\sin[ka'\cos 2\beta\cos(\beta-\varphi)]}{ka'\cos 2\beta(\beta-\varphi)} \quad (4.6)$$

where a' and b' are the illuminated portions of the corner surfaces as shown in figure (4.13). The corresponding scattering functions for H-polarization are obtained from (4.5) and (4.6) after replacing sin $(3\beta \pm \varphi)$ with sin $(3\beta \mp \varphi)$. The normalized RCS for the dihedral corner can now be determined by using (4.3)—(4.6) in (4.2), given by,

$$\frac{\sigma}{d^2} = \frac{1}{4\pi}\left|\sum_{m=1}^{4} R_m \sin(P_m)[\exp(-i2Q_m)-1]/Q_m\right|^2, \quad (4.7)$$

where Q_m, P_m and R_m are shown in table 4.1.

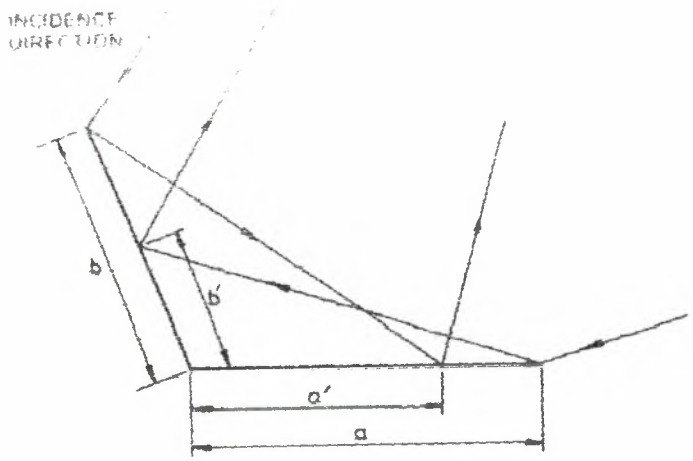

Fig.4.5. Incomplete illumination of face A by wave reflected from face B and vice versa.

m	S	P_m		Q_m	R_m
		E-polarization	*H-polarization*		
1	S_a	$\beta+\varphi$	$\beta+\varphi$	$ka\cos(\beta+\varphi)$	ka
2	S_b	$\beta-\varphi$	$\beta-\varphi$	$kb\cos(\beta-\varphi)$	kb
3	S_{ab}	$3\beta+\varphi$	$-(\beta-\varphi)$	$kb'\cos 2\beta\cos(\beta+\varphi)$	kb'
4	S_{ba}	$3\beta-\varphi$	$-(\beta+\varphi)$	$ka'\cos 2\beta\cos(\beta-\varphi)$	ka'

We can show that the amplitude of the scattered far field due to a dihedral corner with $2\beta \neq \pi/2$ is less than that due to a 90^{o} dihedral corner. The reduction R in the scattered field amplitude can be expressed as,

$$R \cong (kb\sin\tau\cos\gamma_O)^{-1} = (ka\sin\tau\sin\gamma_O)^{-1} \quad , \tag{4.8}$$

where $\tau = 2\beta - \pi/2$ and $\gamma_o = \pi/4 + \varphi$

The reduction factor for a metallic cylindrical segment compared to a rectangular segment shown in Figure 4.6 is given by,

$$R = \frac{\theta}{2}\left(\frac{d}{h} + \frac{h}{d}\right), for \Delta\theta < \gamma \quad , \tag{4.9}$$

$$= 1 for \Delta\theta > \gamma$$

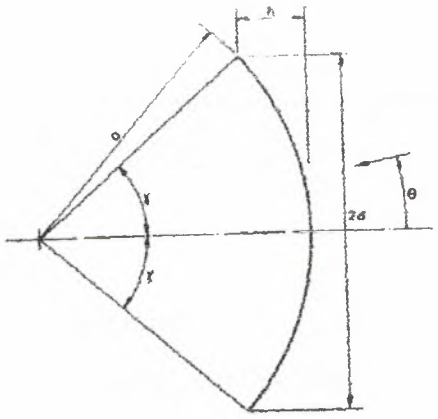

Fig.4.6. Geometry of a cylindrical segment.

where $\Delta\theta$ is the base interval in aspect angles, and d and h are as shown in figure (4.6). Figure (4.7) shows the reduction R versus h /d based on mean returns averaged over the indicated base intervals.

The calculated RCS patterns for dihedral corners in ka = 45 and kb = 30, and $2\beta =$ 100° and 90°, are shown in Figure (4.8), where we find that an RCS reduction of about 17.5 dB is possible around $\varphi = 0°$; that is, when the incidence is along the line bisecting the dihedral angle. There is a minimum reduction of about 12.7 dB in the central angular region bounded by ± 25°. Also note that reduction in RCS is not independent of the size of the corner faces. We therefore recommend that in using the present method we must achieve a specific amount of reduction in RCS at the lowest frequency in the band of frequencies of interest, which will translate to more reduction at the higher frequencies of the band. Further reduction in RCS then can be obtained by using RAM in localized regions.

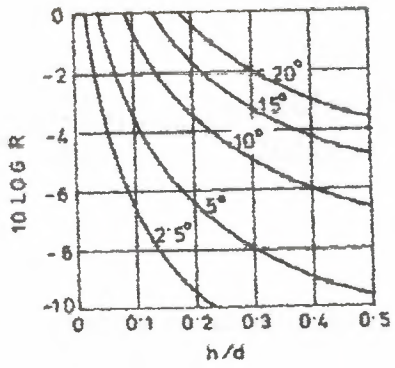

Fig.4.7. Approximate RCS reduction based on mean return averaged over the incident interval.

4.2.2. Plane Surface Made Cylindrical

Large specular returns from a flat metallic plate can be reduced by deforming the plate into a cylindrical plate; however, this method may not reduce the mean RCS by more than 1 dB. The reduction would be appreciable when the angular extent of the plate is considerably larger than the angular sector in which the RCS reduction is desired. The geometry of an electrically large cylindrical structure is shown in Figure 4. 6; its axial length is assumed to be 1.

$$\sigma = \frac{\lambda^2}{\pi}|S|^2 \quad , \tag{4.10-a}$$

$$S = \frac{ik^2}{\pi}\left|\int_A \hat{n}.\hat{i}\,\exp\left(i2\hat{k}r.\hat{i}\right)da\right| \quad , \tag{4.10-b}$$

where

$\hat{i}$ = the unit vector in the direction of incidence,

$\hat{n}$ = the vector normal to the surface at the point incidence,

r = the position vector for the point of incidence on the surface,

da = an elementary area on the surface A.

For a flat plate of length 2d and width 1, the equations above yield the familiar result as below:

$$\sigma_{flatplate} = \frac{l^2}{\pi}\left[2kd\cos\theta\frac{\sin(2kd\sin\theta)}{2kd\sin\theta}\right]^2 , \qquad (4.11)$$

For the cylindrical configuration the equations reduces to:

$$S = ika\exp(-ika)\int_{-(\gamma+\theta)}^{(\gamma-\theta)}\cos\gamma\exp[i2ka(1-\cos\tau)]d\tau \quad , \qquad (4.12)$$

which may be evaluated numerically, if τ is small, $\cos\tau \cong 1-\tau^2/2$, and then (4.12) assumes the following form:

$$S \cong \frac{ika}{\tau}\exp(-ika)\int_{-(\gamma+\theta)}^{(\gamma-\theta)}\exp(ika\tau^2)d\tau \quad , \qquad (4.13)$$

which can be expressed in terms of Fresnel integrals. The RCS for a cylindrical segment can now be determined by using:

$$\sigma_{cyl} = \frac{kal^2}{2}\left|F\left[2\sqrt{a/\lambda}(\gamma-\theta)\right]+F\left[2\sqrt{a/\lambda}(\gamma+\theta)\right]\right|^2 , \qquad (4.14)$$

where

$$F(x) = \int_0^x \exp\left(\frac{j\pi t^2}{2}\right)dt \quad , \qquad (4.15)$$

Figure (4.8) shows the RCS pattern for a cylindrical segment of width $2d = 30\,\lambda$ for a variety of h. The important conclusions that can be drawn from the results shown,

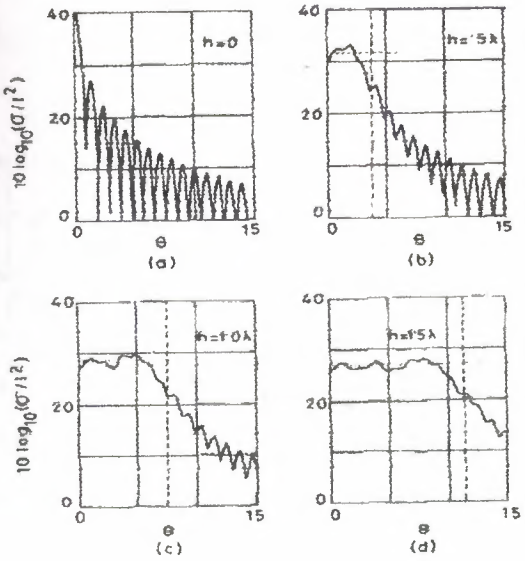

Fig.4.8. RCS patterns of cylindrical segment of half-width $\alpha = 15\lambda$. Dashed lines indicate segment of half-angle γ and dotted lines indicates PO return from curved surface.

In figure (4.8) are these; as the plate becomes more and more curved, the main lobe of the return becomes broadened and reduces in intensity, which means a suppression of the specular echo accompanied by an enhancement for angles in the neighborhood of the specular region. To a radar target RCS control engineer, the mean returns rather than the details of returns are of interest. Figure (4.9a—c) show the mean RCS values for a cylindrical segment obtained by averaging over a given aspect angle interval. Observe from figure (4.9) that the mean RCS is approximately independent of the increase in h until the base interval is equal to y, after which the mean cross section decreases rapidly.

$$R = \frac{\Delta\theta}{2}\left(\frac{d}{h}+\frac{h}{d}\right), \theta\langle\gamma$$
$$\approx 1, \theta\rangle\gamma$$

with

$$a = \frac{d}{2}\left(\frac{h}{d}+\frac{d}{h}\right)$$

for a small $\Delta\theta$,

$$R = \frac{\lambda}{16h}\frac{h^2 + d^2}{d^2}, \qquad (4.16)$$

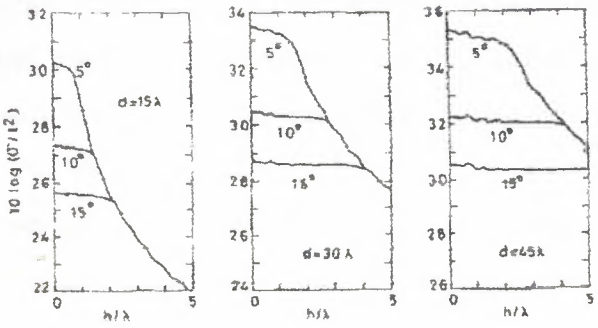

Fig.4.9. Mean RCS obtained by averaging over indicated angular sector for differential values of a interval.

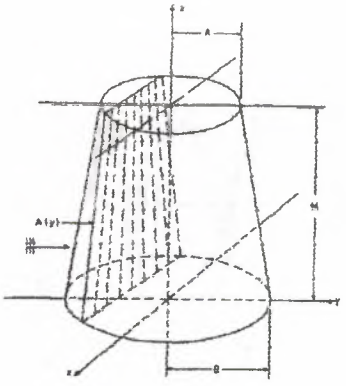

Fig.4.10. A truncated cone.

The RCS reduction is independent of wavelength when the mean RCS is used, but this depends on the aspect angle sector over which the mean is taken. For a small 40, the reduction becomes wavelength dependent. Maximum reduction is possible by replacing the flat plate by a semi-cylinder with h = d in which case R = 40. The essential condition for a cylindrical segment to provide RCS reduction is that it should have an angle larger than the averaging interval.

4.2.3 Shaping of Support Columns

The question of shaping support columns for antennas and scatterers plays an important role because they may cause unwanted reflections. This has been discussed in several references. When fabricated from low-density plastic foam, a truncated cone model support has been found to be superior to a cylindrical column [Geometry of a truncated cone is shown in Figure 4.10; experimental backscattering cross sections for the truncated cone are shown in figure (4.11), which also shows a theoretical backscattering cross section for a circular cylinder for comparison. In applications where dielectric structural support rods must be placed parallel to the electric field vector of an Incident electromagnetic wave, the scattering by such supports can be reduced consider ably by canceling the capacitance with the help of inductive tunes. Measured scattering patterns for the support dielectric post with and without tuning are shown in figure (4.12).

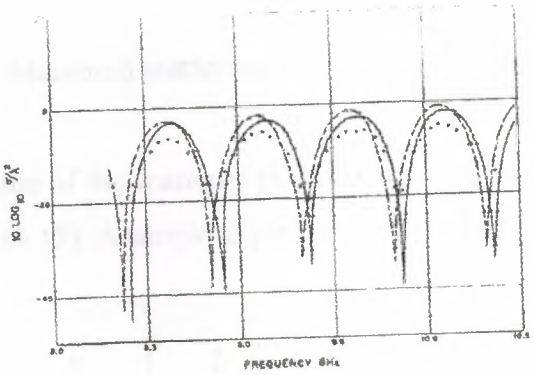

Fig.4.11. Backscattering form a truncated cone (A=15.16cm, β=15.32 cm, M= 39.85 cm) .

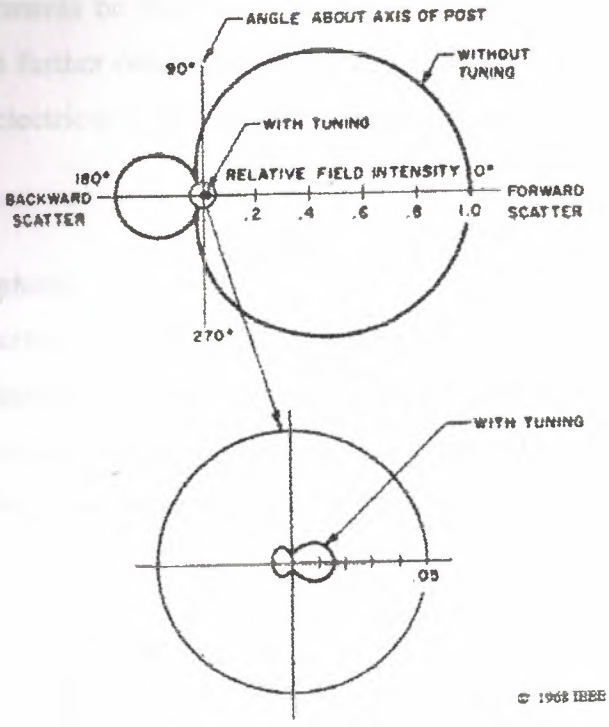

Fig.4.12. Measured scattering field patterns of support post.

Average suppression of the scattered power of the support post by a typical tuning post is shown in figure (4.13). A simple approximate formula tot the radius a of the

$$a = \frac{b}{\sqrt{\varepsilon}} \exp\left[-\frac{2}{k-1} \left(\frac{\lambda}{2\pi b} \right)^2 \right] , \qquad (4.17)$$

where b is the radius of the dielectric post.

The echo widths (RCS per unit length) of dielectric cylinders made of foam material (ε_r= 1.035) and having circular, square, and triangular cross sections have been investigated theoretically and experimentally. The researchers found, in general, that a cylinder with square cross section has an echo width at least 13 dB below that of a cylinder with circular cross section, although a circular cylinder can have low echo width for a narrow band of frequencies. On the basis of these observations it is recommended that dielectric support structures or pedestals used during antenna or

scattering measurements be shaped to have a square cross section. The basis of the recommendation is further confirmed by Figure (4.13 a, b), which gives results for the echo widths for dielectric cylinders having triangular and square cross sections.

4.2.4 The Cone-Sphere

A metallic cone-sphere having a smooth transition between the base of the cone and the spherical section has a low backscattering cross section for some range of aspect angles. For this reason, such configurations have attracted attention for many possible applications, and its scattering properties have been studied in great detail by Senior.

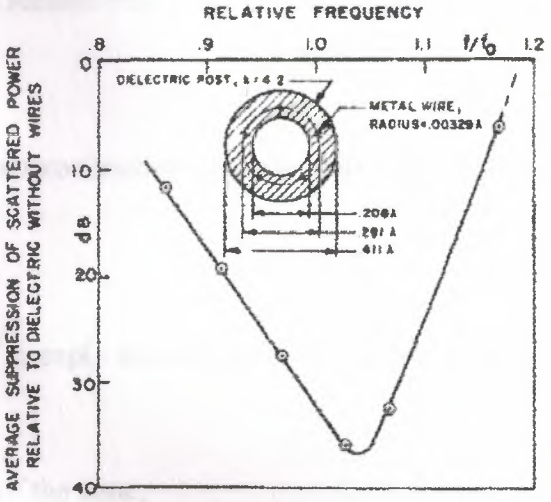

Fig.4.13. Average suppression of scattered power as a function of frequency for the illustration tuned post.

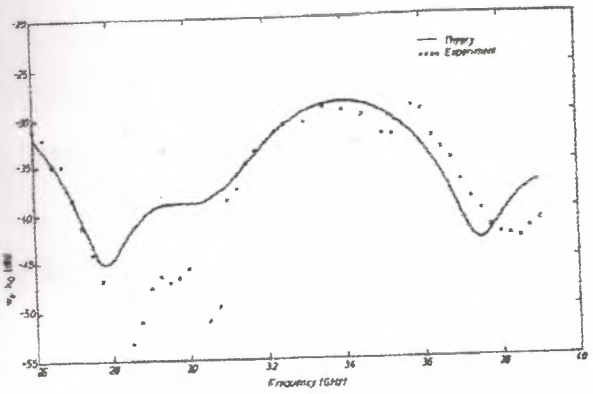

Fig.4.14. (a) The echo width for a cylindrical with triangular cross section multiplied by the free-space propagation constant with frequency. (b) The echo width for a cylinder with square cross section multiplied by the free space propagation constant with frequency.

Physical optics approximation to the nose-on scattering function for a cone-sphere is,

$$S = -\frac{i}{4}\left[\tan^2\alpha \exp(-ika\cos ec\alpha) - \sec^2\alpha \exp(-i2ka\sin\alpha) + 1\right] \quad , \qquad (4.18)$$

where

2α = the total angle of the cone,

a = the radius of the base.

In figure (4.9) the first, second, and third terms may be identified as contributions from the tip, cone-sphere joint, and the shadow boundary, respectively. Further details are available. The shadow boundary contribution given by the PO expression in (4.9) has been found to give incorrect results; analytical expression for this based on creeping wave analysis has been obtained by Senior and Goodrich.

Knott and Senior showed that connecting fins of suitable size makes the cross section depend critically on the roll and aspect angel. It is then possible to significantly reduce the noise-on RCS over small angular sector. Fig (4.15) shows the normalized nose-on RCS versus aspect angle for a cone-sphere ($\theta = 40^0$) with and without fins.

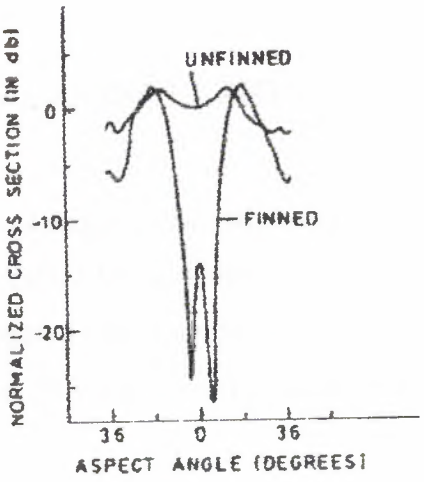

Fig.4.15. The normalized cross section as a function of aspect angle with $\alpha = 40^{o}$ for a cone sphere with and without fins.

The reduction of nose-on RCS by fins is clear from figure (4.15). Generally, we can obtain some reduction in nose-on RCS for all roll angles with particular fin size and at a particular frequency but such reduction is quite small.

CHAPTER 5

CONCLUSION

The power scattered from a target in the direction of the radar receiver, and hence the radar cross section, can be calculated by solving Maxwell's equations with the proper boundary conditions applied or by computer modeling. The radar cross section can also be measured, based on the radar Eq. using either full-size or scale models of targets.

Radar cross section depends on the characteristics dimensions of the object compared to the radar wavelength. When the wavelength is large compared to the object's dimensions, scattering is said to be in the Raleigh region. It is named after Lord Raleigh who first observed this type of scattering in 1871, long before the existence of radar, when investigating the scattering of light by microscopic particles.

The radar cross section is simply and shortly the back bone of radar technology and the working principle without it the radar may not be useful.

LIST OF SYMBOLS

A	Physical area (m^2)
A	Magnetic vector potential $\left(Wb/m\right)$
A_e	Effective aperture (m^2)
a	Radius of loop (m)
	Radius of disk (m)
B	Magnetic flux density $\left(Wb/m^2\right) = T$
b	Length (m)
c	Velocity of light in free space $\left(m/s\right)$
D	Electric flux density vector $\left(C/m^2\right)$
dB	Decibel
dl	Scalar length element (m)
dl	Vector length element (m)
ds	Scalar area element (m^2)
ds	Vector area element (m^2)
dv	Volume element (m^3)
E	Electric field intensity $\left(V/m\right)$
E_x, E_y, E_z	Rectangular components of electric field intensity vector $\left(V/m\right)$
E_θ, E_r, E_φ	Spherical components of electric field intensity vector $\left(V/m\right)$
$E_{II,\perp}$	Parallel and perpendicular components of the electric field intensity $\left(V/m\right)$

G_R, G_T	Gain of receiving , transmitting anteenas
GTD	Geometrical theory of antennas
H	Magnetic field intensity $\left(A/m\right)$
I^e	Equaling electric current (A)
I^m	Equaling magnetic current (V)
$\hat{i}$	$\sqrt{-1}$
J	Volume electric current density $\left(A/m^2\right)$
L_p	Polarization loss factor
n_o	Refractive index of free space
$\hat{n}$	Unit positive normal vector
P_R, P_T	Power received, transmitted
PDF	Probability density function
PTD	Physical theory of diffraction
R	Resistance between receiving antenna and target
$R_{i,j}$	Reflection coefficient at the interface between the medium i and j
R_a	Antenna resistance
RAM	Radar absorbing material
RAS	Radar absorbing surface
RCS	Radar cross section
$S_{(r,\theta,\varphi)}$	Range dependent scattering function
Z_s	Surface impedance
α	Interior angle of the infinite wedge
β	Bistatic angle
$\Gamma(\cdot)$	Gamma function
Γ	Divergence factor
δ	Angle

δ_S	Skin depth of material
ε	Permittivity of a medium
ε'	Real part of ε
ε''	Imaginary part of ε
ε_O	Permittivity of free space
η	Intrinsic impedance of a medium (Ω)
η_O	Intrinsic impedance of free space (Ω)
θ	Angle in spherical coordinate system
λ	Wavelength in a medium (m)
ζ	Measure of chirality in a medium
π	$(= 3.1416)$, Radius of circle
ρ	Cylindrical coordinate
$\sigma_{(r,\theta,\varphi)}$	Range dependent bistatic RCS (m^2)
$\sigma_{(\theta,\varphi)}$	Range independent or far field bistatic RCS (m^2)
φ	Angle in spherical coordinate system
ψ^+	$\varphi + \varphi'$
ψ^-	$\varphi - \varphi'$

REFERENCES

Literature References

1. Introduction to radar systems [Merrill I. Skolnik]

2. Radar cross section analysis and control [Asoke K. Bhattacharyya, D.L. Sengupta]

3. Radar handbook [Miller I. Skolnik]

On-line References

1. www.ieee.com
2. www.yahoo.com
3. www.ask.com
4. www.google.com
5. www.msn.com